Publisher: GSA
Journal: GEOL: Geology
DOI:10.1130/G37382.1

Rapid priming, accumulation, and recharge of magma driving recent eruptions at a hyperactive caldera volcano

Simon J. Barker[1,2*], Colin J.N. Wilson[1], Daniel J. Morgan[3], and Julie V. Rowland[2]

[1]School of Geography, Environment and Earth Sciences, Victoria University, P.O. Box 600, Wellington 6140, New Zealand

[2]School of Environment, University of Auckland, Private Bag 92019, Auckland 1142, New Zealand

[3]School of Earth and Environment, University of Leeds, Leeds LS2 9JT, UK

ABSTRACT

A major challenge in volcanology is determining the factors that control the frequency and magnitude of eruptions at hazardous caldera volcanoes. Understanding the critical sequence of events that may lead to future eruptions is vital for volcanic monitoring and risk assessment. Here we use magma chemistry and mineral diffusion modeling to interpret the magmatic processes and timescales involved in the youngest three eruptions (2.15- 1.7 ka) from Taupo volcano (New Zealand), that peaked with the voluminous 232 AD eruption. Of the rhyolites erupted since ~12 ka, the <2.15 ka magmas have the lowest whole-rock SiO_2 content and reversely-zoned crystals, yet with high-SiO_2 melt inclusions. Mineral zonations and compositional shifts reflect a 30–40 °C temperature increase over the immediately preceding (>2.75 ka) rhyolites that were tapped from the same magma reservoir. Orthopyroxene Fe-Mg diffusion timescales indicate that the onset of rapid heating and priming of the host silicic mush occurred <120 years prior to the <2.15 ka eruptions, with subsequent melt accumulation occurring

Publisher: GSA
Journal: GEOL: Geology
DOI:10.1130/G37382.1

in only decades. Elevated mafic magma supply to the silicic mush pile, rapid melt accumulation and high differential tectonic stress built up and culminated in the ~105 km^3 232 AD eruption, one of the largest and most violent Holocene eruptions globally. These youngest eruptions demonstrate how Taupo's magmatic system can rapidly change behavior to generate large eruptible melt bodies on timescales of direct relevance to humans and monitoring initiatives.

INTRODUCTION

In their stratigraphic records, caldera volcanoes commonly display a wide range of eruptive styles, from small dome-building events through to large explosive, caldera-forming events. However, relationships between eruptive frequency and magnitude are often chaotic, rather than linear, making the forecasting of future activity (timing, volume) inherently problematic (e.g., Wilson, 1993). In addition, perceptions of the behavior of large silicic caldera volcanoes based on their past activity mean that significant unrest episodes with no eruption, or the onset of volcanic activity (regardless of its actual magnitude), could trigger overwhelming socio-economic consequences (e.g., Lowenstern et al., 2006). The productivity of caldera volcanoes and their inducement into eruption can be governed by internal processes including magma recharge (Blake et al., 1992), magma overpressure or buoyancy (Caricchi et al., 2014) and/or external factors, such as changes in regional stress states (Rowland et al., 2010). Central to understanding eruption onsets and behavior is linking patterns in past activity to changes in magmatic processes over measurable pre-eruptive timescales.

Taupo volcano (Fig. 1) is a large silicic caldera that hosted the Oruanui supereruption at 25.4 ka, which evacuated >1100 km^3 of pyroclastic material (Allan et

al., 2013). From 21.5 to 17 ka Taupo produced 3 dacitic eruptions, and then from 12 to 1.7 ka, 25 rhyolite eruptions spanning 3–4 orders of magnitude in volume (Wilson, 1993). Sutton et al. (1995) split the post-Oruanui rhyolites (labelled B through Z) into three chemically distinct subgroups: SG1 (12–10 ka), SG2 (7–2.75 ka) and SG3 (2.15–1.7 ka). SG3, represented by three eruptions (X-Z), is of key importance in establishing the magmatic state of the modern volcano. The first (eruption X) was of moderate volume (~0.8 km^3 pyroclastic material) and from a vent site geographically overlapping that of earlier eruption V (SG2: Fig. 1). Only ~430 years later at 232 ± 5 AD (Hogg et al., 2011), eruption Y discharged 2–3 times the volume (105 km^3) of all other post-Oruanui eruptions combined. Based on eruptive style and intensity changes, the associated Unit Y pyroclastic deposits have been split into seven subunits (Y1-Y7: Fig. 1). Several years to decades later the subaqueous dome-forming eruption Z (0.3 km^3) was the last known activity. With its young deposits, overlapping vent sites and high eruptive frequency, Taupo provides a unique opportunity to investigate magmatic and eruptive behavior at a hyperactive caldera volcano.

Numerous studies have highlighted that rather than being long-lived, melt-dominant magma bodies are transient features in silicic magmatic systems, which instead are dominated by regions of variably crystalline mush (e.g., Caricchi and Blundy, 2015 and references therein). Processes generating crystal-poor rhyolites, such as those erupted at Taupo, must therefore involve the extraction of rhyolite melt from a crystal mush, accumulation of a melt-dominant body, and its eruption prior to significant cooling and crystallization. Large volumes of crystal mush have been invoked to explain development of the Oruanui magma body (Allan et al., 2013), and significant volumes of mush are

likely to have been re-established into the modern system (>200–1000 km^3: Barker et al., 2015). Here we examine the three youngest eruptions at Taupo, using trends in magma chemistry and mineral diffusion modeling to interpret the pre-eruptive timing and development of their crystal-poor magma bodies.

CHARACTERISTICS OF THE YOUNGEST TAUPO MAGMAS

The SG3 rhyolites are the least evolved in the post-Oruanui sequence. Whole-rock compositions for units X, Y and Z are up to ~1% lower in SiO_2 than the final eruptions of SG2 prior to 2.75 ka (U, V and W: Fig. 2a). The first erupted Y subunits are the most evolved (up to ~74.5 wt. % SiO_2), and eruption Z lava is the least evolved (~73.5 wt. %), although groundmass glasses in all SG3 pumices are uniformly 74.5–75.5 wt. % SiO_2. Melt inclusions (MIs) in SG3 orthopyroxene and plagioclase are significantly more evolved, however, at up to 77 wt. % SiO_2, overlapping compositionally with SG2 groundmass glasses. Whole-rock compositions show stepwise temporal changes in Rb/Sr ratio (Fig. 2b), and increases in compatible trace elements between SG2-SG3 (e.g., Sr and Eu for plagioclase; Zn and Mn for orthopyroxene: Tables DR1 and DR2 in the GSA data repository[1]).

Mineral textures and compositions also contrast between SG2 and SG3 eruption products. SG2 crystals are euhedral with only minor normal compositional zoning (Figs DR1-DR8 in the GSA data repository[1]). In contrast, Unit X is dominated (~85%) by reversely zoned orthopyroxene and plagioclase with narrow resorbed rims (<20–30µm: Fig. 3), with only ~15% of strongly normally zoned crystals. Notably, the core compositions of reversely zoned crystals overlap with those of their SG2 counterparts. Unit Y orthopyroxenes have the widest rims (90 µm), and rim compositions on both

Publisher: GSA
Journal: GEOL: Geology
DOI:10.1130/G37382.1

normally and reversely zoned crystals are identical. Eruption Z crystals display similar textural features to Y but its products contain additional high-An plagioclase (up to An_{98}) as individual crystals and within mafic enclaves accompanying rare olivine up to Fo_{90} (Barker et al., 2015).

Given the geographic overlap of vents, and matching melt inclusion and crystal core compositions in the SG2-SG3 products, we infer that they tapped similar regions of Taupo's silicic mush reservoir. The SG2-SG3 transition coincides with a shift in $^{87}Sr/^{86}Sr$ ratios from ~0.7062 to ~0.7060 (Sutton et al., 1995), suggesting that SG3 magmas reflect less assimilation of Mesozoic metasedimentary country rock, or that the SG3 magmatic system was modified through an influx of less radiogenic magma, accompanying the changing crystal growth profiles (Fig. 3). As SG3 Fe-Ti oxide model temperatures display a 30–40 °C increase from SG2 temperatures (Barker et al., 2015), the contrasting SG2-SG3 mineral textures can be best explained by elevated temperatures, with reversely zoned SG3 orthopyroxenes inheriting low-Mg cores and high-SiO_2 MIs from the earlier SG2 magmatic system.

TIMESCALES OF HEATING

The ~600 year time gap between Unit W (>2.75 ± 0.1 ka) and Unit X (2.15 ± 0.07 ka: Wilson, 1993) provides a maximum duration for heating and compositional changes before the SG3 eruptions. Diffusion modeling is used here to refine this timing. Diffusion modeling assumes compositional boundaries initially had step-wise gradients, which were modified by diffusion to form sigmoidal concentration gradients until eruptive quenching (e.g., Morgan et al., 2004). SG3 orthopyroxene displays narrow (<50 µm) diffusion profiles in back-scattered electron (BSE) images along the crystallographic a-

Publisher: GSA
Journal: GEOL: Geology
DOI:10.1130/G37382.1

and b-axes in both interior normally zoned cores and reversely zoned rims (Figs. DR9-DR13 in the GSA data repository[1]). We have modeled Fe-Mg diffusion in orthopyroxene to match observed profiles (Fig. 3), with $D_{Fe\text{-}Mg}$ from Ganguly and Tazzoli (1994) corrected for fO_2 dependence (following Allan et al., 2013). The maximum diffusion timescale for Unit X orthopyroxene is ~120 years, with averages for normally zoned crystals of ~50 years, and reversely zoned crystals all <30 years (Fig. 4). Similar ranges are derived for the Unit Y subunits, with no major differences between subunits or crystal zonation type. The maximum timescale for Unit Y is ~350 years, but most estimates are <100 years (Fig. 4). Eruption Z timescales overlap with the Unit Y eruption age, with the youngest observed diffusion ages being less than a decade.

DISCUSSION

What Caused Rapid Heating of Taupo's Silicic Magmatic System?

The changes in SG2-SG3 whole-rock chemistry and mineral zonation patterns with their increasing temperature signals indicates that there was heating and consequent compositional shifts during the ~600 year break, interpreted to reflect enhanced interaction between mafic magmas and the silicic system. Such interactions, prior to or during eruption, are common in the Taupo Volcanic Zone (TVZ) (Wilson et al., 2009). At Taupo, streaky pumices and scoria in the 3.5 ka Unit S (SG2) deposit reflect mixing between cooler rhyolite (830 °C) and hotter andesite (~1100 °C) (Blake et al., 1992). Products of eruptions X and Y, however, display little physical evidence for direct mafic interaction. Eruption Z material, in contrast, contains dark gray enclaves with high-An plagioclase and olivine xenocrysts, indicating that primitive, mantle-derived (Fo_{90}), high-Mg magmas were reaching the silicic system (cf. Gamble et al., 1990). We infer that

Publisher: GSA
Journal: GEOL: Geology
DOI:10.1130/G37382.1

there is a spectrum of possible interactions between mafic melts and the silicic magmatic system, depending on the timing of mafic magma injection with respect to the physical state of the overlying silicic mush. Prior to eruption S, crystal-poor andesite penetrated the silicic mush and flowed across the floor of a crystal-poor rhyolite body (i.e., the underlying mush was 'solid') and was physically mixed to form hybrid rhyodacite (Blake et al., 1992). In eruptions X and Y, the mafic component did not intersect a crystal-poor magma body, but may have penetrated into the mush system via diking and fracturing, driving heating, large scale overturn and mobilization (e.g., Bain et al., 2013). In eruption Z, the mafic component once again interacted with a crystal-poor rhyolite magma body.

Mechanisms and Rates of Pre-Eruptive Magma Priming, Melt Extraction, and Accumulation

If the heating episode(s) recorded in SG3 crystals are attributed to mafic magma priming, the timing and mechanisms of this process can be constrained by the diffusive timescales. The model ages within individual eruptions range from decades to centuries and we consider this to reflect variable crystal histories of mafic interaction, with crystals in close proximity to the heat source being resorbed first during the onset of heating and temporary mineral disequilibrium in the silicic mush (~100–350 years: Fig. 4). At least ~10%–15% of the volume of the relatively cool rhyolite magmas (~830 °C) would be required in the form of hot (~1100 °C) mafic magmas to cause the recorded 30–40 °C temperature increase. For the ~35 km^3 DRE eruption Y magma body, this equates to a ~0.03–0.05 km^3 yr^{-1} mafic magma influx over ~100 years. These estimates of mafic flux are minima given the relatively low efficiency of heat transfer during dike intrusion (e.g., Snyder, 2000) and the large inferred volume (200–1000 km^3) of the silicic mush reservoir

Publisher: GSA
Journal: GEOL: Geology
DOI:10.1130/G37382.1

beneath Taupo (Barker et al., 2015). Mafic magma infiltration is inferred to have occurred through multiple episodes of diking, given the lack of overlapping diffusion ages between eruptions X and Y and fresh mafic enclaves observed in eruption Z lavas, with heating and disruption most pronounced before eruption Y. Our findings highlight two important features of Taupo's magmatic system. First, mafic supplies and styles of interaction with the silicic magmatic system may be highly variable through time. Second, elevated mafic supplies may result in priming and significant changes to the silicic magmatic system (and its crystal cargo) in only hundreds of years.

The relative timing of melt extraction from the primed crystal mush can then, in turn, be constrained by temporal changes in magma and mineral compositions. Stepwise changes in composition between the SG2 and SG3 rhyolites (Fig. 2) are consistent with 5%–10% dissolution of orthopyroxene and plagioclase, liberating compatible trace elements (e.g., Sr, Eu, Zn, Mn, Ti) from the crystals to the melt phase within the crystal mush (Barker et al., 2015). These signatures would only be recorded in the final SG3 eruptive products if heating and dissolution occurred in the mush prior to extraction of the crystal-poor rhyolite melt (Fig. 2). Notably, rapid heating by 30–40 °C would reduce the viscosity of interstitial rhyolite melt by a factor of ~2 for SG3 glass compositions (Table DR2 in the GSA data repository[1]), aiding the movement of melt as its proportions increased in the mush (e.g., Bain et al., 2013; Caricchi et al., 2014). We therefore use the shortest diffusive timescales (~5–20 years: Fig. 4) to constrain a maximum timescale for melt extraction and subsequent shallow-level accumulation of the pre-eruptive crystal-poor rhyolite melt body. Short timescales of shallow melt storage are in agreement with the apparent homogeneity of magma chemistries and uniform crystal rim compositions

Publisher: GSA
Journal: GEOL: Geology
DOI:10.1130/G37382.1

between the beginning and end of individual eruptions (Figs. 2A, 3), consistent with little or no pre-eruptive zoning in the magma body that would result from significant cooling and crystallization.

The shortest diffusion profiles yield a first-order rate estimate for the accumulation of crystal-poor magma bodies prior to the SG3 eruptions. Using the shortest diffusion age of ~10 years, eruption X represents a melt accumulation rate of ~0.03 km^3/year (Fig. 4). In contrast, eruption Y yields a rate of ~3.5 km^3/year, comparable to that inferred for the Oruanui supereruption (Allan et al., 2013). These accumulation rates highlight two further features of Taupo's magmatic system. First, large volumes of eruptible crystal-poor magma can be assembled on timescales of decades that are relevant to volcanic monitoring. Second, Taupo can rapidly generate multiple eruptions of similar composition, with diffusion timescales in eruption Z overlapping with eruption Y several years to decades earlier (Fig. 4), emphasising the rapid response of the magmatic system to subsequent magma recharge and disruption (cf. Till et al., 2015).

The rapid rates of magma priming and melt accumulation raise questions about the controls on volcanism at Taupo. For example, how did 35 km^3 of crystal-poor magma accumulate for eruption Y without being released earlier with a smaller volume? Eruption Y was spasmodic and involved multiple vents (Fig. 1), with similar magma compositions throughout (Figs. 2, 3). In such a case, the controls on volcanism cannot simply be linked to magma-driven overpressure or buoyancy. As demonstrated by Allan et al. (2012), rifting played a major role in modulating the Oruanui supereruption. Here we note that the SG3 vents also form a NE-striking alignment perpendicular to the far-field extension

direction. The inferred rates of mafic magma supply for the SG3 eruptions are comparable to those in the 2005–2012 Afar and the 1975–1984 Krafla rifting episodes (e.g., Ebinger et al., 2010). Such episodes appear to occur over length scales of several tens of kilometers and the far field extension rate in these localities is achieved by punctuated episodes of enhanced seismic, magmatic, and volcanic activity over timescales of centuries. The estimated volumes of intruded mafic and erupted felsic magma at Taupo suggest that the timing and volume of silicic volcanism in general and events like eruption Y in particular can be linked to three independent factors within the TVZ rifted arc setting. These factors are high differential tectonic stresses, variable mafic magma fluxes, and the physical state or readiness of the silicic mush system to produce eruptible melt-dominant magma bodies (Rowland et al., 2010). For eruption Y, a critical combination of these three factors generated one of the largest and most violent Holocene eruptions on Earth.

Implications for Future Activity at Taupo Volcano

The inferred mechanisms driving recent volcanism at Taupo, and their timescales of occurrence, have two implications for ongoing monitoring and hazard mitigation. First, magmatic processes can occur over timescales that are relevant to humanity. The eruptions considered here resulted from mafic priming of the silicic mush system over centuries, and accumulation of the eruptible magma bodies over decades or less. Second, there are multiple controls on the timing and volume of eruptions, with complex relationships between the deep mafic system, the shallower silicic mush system and tectonic stresses. Multiple seismic swarms occurred at Taupo during 1922, 1964–65 and 1983 and were accompanied by surface deformation, modeled for the post-1983 period as

'dewatering' of a ~2.5 km^3 intrusion at ~8 km depth (Smith et al., 2007). These events suggest that magma bodies are being emplaced in the modern system. However, consideration of future activity at Taupo is challenging due to uncertainties involved with the nature of events that occur as background processes in an area of active rifting, versus those that may herald future eruptions. The hyperactive but widely variable behavior of Taupo highlights the importance of future monitoring and seeking to determine what separates 'normal' cyclic unrest events at a restless caldera from a critical sequence of events that could lead to future eruption(s).

ACKNOWLEDGMENTS

We thank John Gamble, Roger Briggs, Michelle Coombs, George Cooper and Katy Chamberlain for helpful discussions and Stephen Self, Kate Saunders, Richard Price, Mark Jellinek and two anonymous reviewers for insightful reviews. We also acknowledge the Marsden Fund of the RSNZ (Grant VUW0813), a James Cook Fellowship to CJNW, and a VUW Doctoral Scholarship awarded to SJB.

REFERENCES CITED

Allan, A.S.R., Wilson, C.J.N., Millet, M.-A., and Wysoczanski, R.J., 2012, The invisible hand: Tectonic triggering and modulation of a rhyolitic supereruption: Geology, v. 40, p. 563–566, doi:10.1130/G32969.1.

Allan, A.S.R., Morgan, D.J., Wilson, C.J.N., and Millet, M.-A., 2013, From mush to eruption in centuries: Assembly of the super-sized Oruanui magma body: Contributions to Mineralogy and Petrology, v. 166, p. 143–164, doi:10.1007/s00410-013-0869-2.

252 Bain, A.A., Jellinek, A.M., and Wiebe, R.A., 2013, Quantitative field constraints on the
253 dynamics of silicic magma chamber rejuvenation and overturn: Contributions to
254 Mineralogy and Petrology, v. 165, p. 1275–1294, doi:10.1007/s00410-013-0858-5.
255 Barker, S.J., Wilson, C.J.N., Allan, A.S.R., and Schipper, C.I., 2015, Fine-scale temporal
256 recovery, reconstruction and evolution of a post-supereruption magmatic system:
257 Contributions to Mineralogy and Petrology, v. 170, article 5, doi:10.1007/s00410-
258 015-1155-2.
259 Blake, S., Wilson, C.J.N., Smith, I.E.M., and Walker, G.P.L., 1992, Petrology and
260 dynamics of the Waimihia mixed magma eruption, Taupo Volcano, New Zealand:
261 Journal of the Geological Society [London], v. 149, p. 193–207,
262 doi:10.1144/gsjgs.149.2.0193.
263 Caricchi, L., and Blundy, J., 2015, The temporal evolution of chemical and physical
264 properties of magmatic systems, in Caricchi, L., and Blundy, J., eds., Chemical,
265 physical and temporal evolution of magmatic systems: Geological Society of London
266 Special Publications 422, p. 1–15, doi:10.1144/SP422.11.
267 Caricchi, L., Annen, C., Blundy, J., Simpson, G., and Pinel, V., 2014, Frequency and
268 magnitude of volcanic eruptions controlled by magma injection and buoyancy:
269 Nature Geoscience, v. 7, p. 126–130, doi:10.1038/ngeo2041.
270 Ebinger, C., Ayele, A., Keir, D., Rowland, J., Yirgu, G., Wright, T., Belachew, M., and
271 Hamling, I., 2010, Length and timescales of rift faulting and magma intrusion: the
272 Afar rifting cycle from 2005 to present: Annual Review of Earth and Planetary
273 Sciences, v. 38, p. 439–466, doi:10.1146/annurev-earth-040809-152333.

Gamble, J.A., Smith, I.E.M., Graham, I.J., Kokelaar, B.P., Cole, J.W., Houghton, B.F., and Wilson, C.J.N., 1990, The petrology, phase relations and tectonic setting of basalts from the Taupo Volcanic Zone, New Zealand and the Kermadec Island Arc - Havre Trough, SW Pacific: Journal of Volcanology and Geothermal Research, v. 43, p. 253–270, doi:10.1016/0377-0273(90)90055-K.

Ganguly, J., and Tazzoli, V., 1994, Fe^{2+}-Mg interdiffusion in orthopyroxene: Retrieval from the data on intracrystalline exchange reaction: American Mineralogist, v. 79, p. 930–937.

Hogg, A.G., Lowe, D.J., Palmer, J., Boswijk, G., and Bronk Ramsey, C., 2011, Revised calendar date for the Taupo eruption derived by ^{14}C wiggle-matching using a New Zealand kauri ^{14}C calibration data set: The Holocene, v. 22, p. 439–449, doi:10.1177/0959683611425551.

Lowenstern, J.B., Smith, R.B., and Hill, D.P., 2006, Monitoring super-volcanoes: Geophysical and geochemical signals at Yellowstone and other large caldera systems: Royal Society of London Philosophical Transactions, ser. A, v. 364, p. 2055–2072, doi:10.1098/rsta.2006.1813.

Morgan, D.J., Blake, S., Rogers, N.W.B., DeVivo, B., Rolandi, G., Macdonald, R., and Hawkesworth, C.J., 2004, Time scales of crystal residence and magma chamber volume from modelling of diffusion profiles in phenocrysts: Vesuvius 1944: Earth and Planetary Science Letters, v. 222, p. 933–946, doi:10.1016/j.epsl.2004.03.030.

Rowland, J.V., Wilson, C.J.N., and Gravley, D.M., 2010, Spatial and temporal variations in magma-assisted rifting, Taupo Volcanic Zone, New Zealand: Journal of

Volcanology and Geothermal Research, v. 190, p. 89–108, doi:10.1016/j.jvolgeores.2009.05.004.

Smith, E.G.C., Williams, T.D., and Darby, D.J., 2007, Principal component analysis and modeling of the subsidence of the shoreline of Lake Taupo, New Zealand, 1983–1999: Evidence for dewatering of a magmatic intrusion?: Journal of Geophysical Research, v. 112, B08406, doi:10.1029/2006JB004652.

Snyder, D., 2000, Thermal effects of the intrusion of basaltic magma into a more silicic magma chamber and implications for eruption triggering: Earth and Planetary Science Letters, v. 175, p. 257-273, doi:10.1016/S0012-821X(99)00301-5.

Sutton, A.N., Blake, S., and Wilson, C.J.N., 1995, An outline geochemistry of rhyolite eruptives from Taupo volcanic centre, New Zealand: Journal of Volcanology and Geothermal Research, v. 68, p. 153–175, doi:10.1016/0377-0273(95)00011-I.

Till, C.B., Vazquez, J.A., and Boyce, J.W., 2015, Months between rejuvenation and volcanic eruption at Yellowstone caldera, Wyoming: Geology, v. 43, p. 695–698, doi:10.1130/G36862.1.

Wilson, C.J.N., 1993, Stratigraphy, chronology, styles and dynamics of late Quaternary eruptions from Taupo volcano, New Zealand: Royal Society of London Philosophical Transactions, ser. A, v. 343, p. 205–306, doi:10.1098/rsta.1993.0050.

Wilson, C.J.N., Gravley, D.M., Leonard, G.S., and Rowland, J.V., 2009, Volcanism in the central Taupo Volcanic Zone, New Zealand: Tempo, styles and controls, in Thordarson, T., Larsen, G., Self, S., Rowland, S., and Hoskuldsson, A., eds., Studies in Volcanology: The Legacy of George Walker: Special Publications of IAVCEI, v. 2, p. 225–247.

Publisher: GSA
Journal: GEOL: Geology
DOI:10.1130/G37382.1

FIGURE CAPTIONS

Figure 1. Map of Lake Taupo and the structural and volcanic features of Taupo caldera, New Zealand (map inset). Vent sites with error ellipse, vent envelopes, and ages for the post-Oruanui eruptions are after Wilson (1993).

Figure 2. Variations between the SG3 magmas (eruptions X, Y, Z) and the youngest SG2 magmas (eruptions U, V, W) for (A) major element whole-rock (WR), pumice glass and melt inclusion (MI) compositions, and (B) trace element WR compositions (after Barker et al., 2015). See [1]GSA Data Repository file for geochemical data tables.

Figure 3. Representative back-scattered electron (BSE) images (left) and corresponding Fe-Mg diffusion models (right) of reversely zoned orthopyroxene (OPX) from SG3 units X, Y, and Z. Dashed white boxes in BSE images represent modeling areas. Solid black curves represent the modeled profile of an initially sharp compositional boundary and diamond symbols represent grayscale-calibrated composition with Mg# calculated as Mg = 100*Mg/Mg+Fe_{total} (Allan et al., 2013). Dashed gray line represents the average composition of SG2 OPX rims. Average (Av) diffusion model timescales given for parameter estimates of 860 °C, 1.5 MPa and log fO_2 of 0.2 ΔNNO for eruptions X and Y, and 0.0 ΔNNO for Z are from Barker et al. (2015). Maximum (Max) and minimum (Min) timescales use uncertainties of ± 30 ºC or ± 0.3 log units ΔNNO. See [1]GSA Data Repository for methods, diffusion images and profiles.

Publisher: GSA
Journal: GEOL: Geology
DOI:10.1130/G37382.1

Figure 4. Model timescale estimates (log-scale) of Fe-Mg inter-diffusion in orthopyroxene from the SG3 eruptions and eruption Y subunits. Symbols represent average diffusion timescales, and horizontal lines represent the range between maximum and minimum estimates using the same parameters as for Fig. 3. N denotes crystals with normal zonation. Solid light gray and dark gray vertical lines represent the relative dates of earlier eruptions from SG2 (U-W) and eruption X, respectively.

[1]GSA Data Repository item 2015xxx, geochemical data tables, mineral zoning, diffusion images and profiles are available online at www.geosociety.org/pubs/ft2015.htm, or on request from editing@geosociety.org or Documents Secretary, GSA, P.O. Box 9140, Boulder, CO 80301, USA.

Figure 1

Click here to download Figure Barker et al. Figure 1.pdf

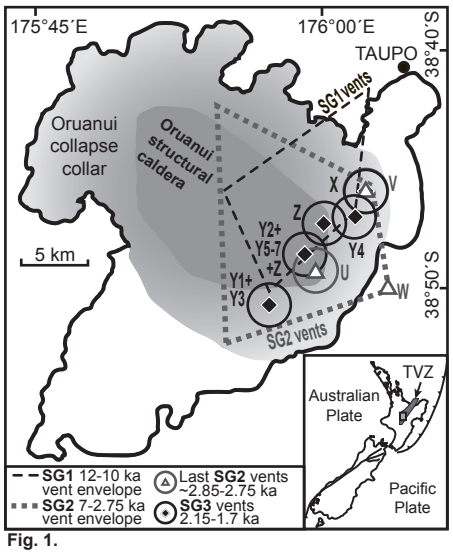

Fig. 1.

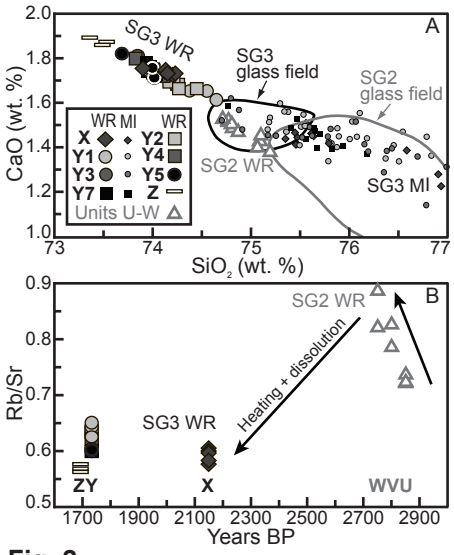

Fig. 2.

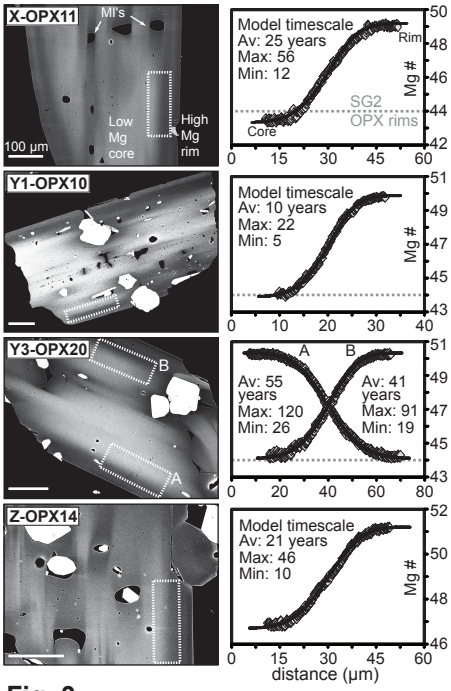

Fig. 3.

Figure 4

Click here to download Figure Barker et al. Figure 4_smaller.pdf

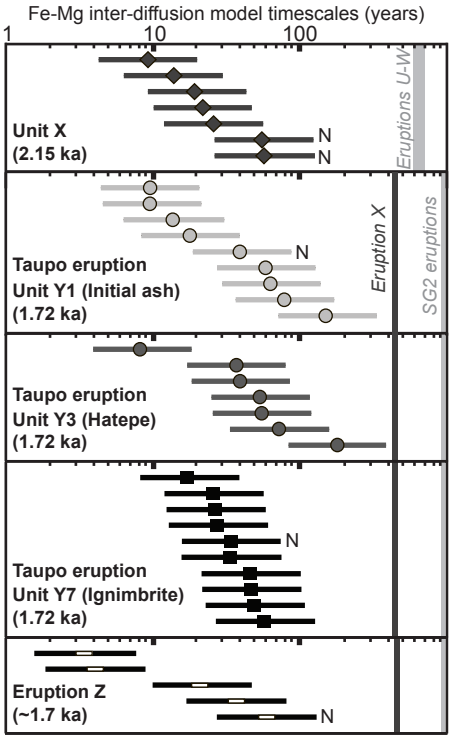

Table DR1. Major and trace element compositions of whole rock (WR) pumices and lava from the final SG2 eruptions (U, V and W) and the SG3 eruptions (X,Y and Z)

Unit	U	U	U	U	U	V	V	V	W	W	W	X1
SG	2	2	2	2	2	2	2	2	2	2	2	3
Sample	P2150A	P2150B	P2150C	P2151	P2152	P2161A	P2162	P2162A	P2155A	P2155B	P2156	P2157
Age BP	2850	2850	2850	2850	2850	2800	2800	2800	2750	2750	2750	2150
WR major elements (wt. %)												
SiO_2	74.76	74.81	74.55	74.77	74.81	74.71	75.09	75.10	75.06	74.87	75.19	73.90
TiO_2	0.25	0.24	0.26	0.25	0.24	0.25	0.24	0.24	0.24	0.24	0.24	0.29
Al_2O_3	13.34	13.24	13.28	13.29	13.21	13.32	13.17	13.21	13.11	13.25	13.05	13.60
Fe_2O_3	2.34	2.36	2.44	2.37	2.37	2.35	2.31	2.29	2.28	2.35	2.29	2.56
MnO	0.085	0.088	0.085	0.088	0.090	0.089	0.086	0.085	0.086	0.086	0.086	0.095
MgO	0.24	0.25	0.31	0.26	0.26	0.26	0.22	0.23	0.23	0.24	0.22	0.35
CaO	1.52	1.50	1.65	1.53	1.51	1.54	1.44	1.46	1.41	1.48	1.39	1.76
Na_2O	4.55	4.58	4.55	4.55	4.60	4.56	4.49	4.48	4.60	4.51	4.54	4.63
K_2O	2.88	2.89	2.82	2.84	2.87	2.88	2.91	2.87	2.94	2.94	2.95	2.76
P_2O_5	0.038	0.043	0.046	0.042	0.041	0.043	0.043	0.045	0.042	0.046	0.041	0.057
LOI	2.34	1.38	0.77	1.72	0.73	2.6	2.96	2.84	0.42	3.18	0.47	2.2
Total	98.9	99	99.59	99.56	98.94	99.14	99.25	99.51	99	99.75	99.02	99.11
WR trace elements (ppm)												
Li	42.30		43.72	41.25		33.61	34.49		33.69	37.49	47.13	
Sc	11.5		11.7	11.1		10.2	10.4		10.1	10.6	12.2	
V	2		7	2		1	2		2	1	3	
Cr	1.9		4.0	2.5		2.3	4.3		2.7	1.4	3.4	
Ni	0.1		0.3	0.1		0.2	0.4		0.3	0.1	0.2	
Cu	1.2		1.5	1.2		1.0	1.3		1.5	1.3	1.4	
Zn	72		72	70		65	65		63	66	78	
Ga	16.8		16.8	16.6		15.1	15.7		15.2	15.6	17.3	
Rb	104.9		104.0	102.0		96.2	100.7		99.6	103.4	103.1	
Sr	142		144	140		122	121		121	116	170	
Y	34.6		33.3	32.8		31.0	32.4		31.5	32.7	35.1	
Zr	210		206	212		189	182		188	182	236	
Nb	9.8		9.6	9.4		7.7	8.0		7.9	8.1	9.8	
Cs	5.19		5.07	5.00		5.05	5.38		5.23	5.30	5.21	
Ba	650		639	631		571	598		588	614	632	
La	26.9		26.1	26.0		23.8	24.8		24.3	25.0	26.9	
Ce	56.8		55.4	55.1		51.2	52.6		52.7	54.0	57.9	
Pr	6.76		6.54	6.46		6.02	6.29		6.16	6.39	6.95	
Nd	26.2		25.9	25.9		23.4	24.8		23.9	24.8	28.0	
Sm	5.73		5.66	5.65		5.06	5.40		5.20	5.41	5.98	
Eu	1.32		1.28	1.31		1.14	1.21		1.17	1.21	1.39	
Gd	6.01		5.83	5.84		5.48	5.97		5.57	6.03	6.54	
Tb	0.92		0.88	0.88		0.81	0.88		0.84	0.87	0.95	
Dy	5.90		5.84	5.82		5.15	5.52		5.21	5.44	6.03	
Ho	1.24		1.18	1.20		1.08	1.14		1.11	1.15	1.27	
Er	3.60		3.45	3.45		3.14	3.34		3.27	3.40	3.59	
Tm	0.539		0.527	0.531		0.470	0.502		0.497	0.512	0.573	
Yb	3.57		3.54	3.51		3.12	3.32		3.26	3.39	3.65	
Lu	0.548		0.535	0.538		0.480	0.512		0.490	0.507	0.552	
Hf	5.82		5.66	5.83		4.97	5.05		5.17	5.11	6.33	
Pb	22.7		22.4	22.7		15.5	16.7		16.6	16.6	22.9	
Th	11.25		10.98	10.99		9.61	10.27		10.24	10.42	11.20	
U	2.50		2.44	2.44		2.18	2.32		2.27	2.31	2.44	
Rb/Sr	0.74		0.72	0.73		0.79	0.83		0.82	0.89	0.60	
Eu/Eu*	0.69		0.68	0.70		0.66	0.65		0.66	0.65	0.68	

Oxide abundances normalised to 100 % on a volatile free basis, with original analytical totals and LOI (loss on ignition) values given. Eruption ages are given in years before present (BP) and sourced from Wilson (1993) and Hogg et al. (2012). Eu/Eu* calculated as Eu / √(Sm*Gd), normalised to chondrite. Major elements analysed by X-Ray Flourescence (XRF) and trace elements by solution Inductively Coupled Plasma Mass Spectrometry (ICPMS). See Barker et al. (2015) for full description of analytical methods and standards.

Table DR1. continued

Unit	X1	X1	X2	X2	X2	Y1	Y1	Y1	Y1	Y2	Y2	Y2
SG	3	3	3	3	3	3	3	3	3	3	3	3
Sample	P2157A	P2157B	P2158	P2158A	P2158B	P2118	P2119	P2120	P2121	P2129	P2130	P2275
Age BP	2150	2150	2150	2150	2150	1720	1720	1720	1720	1720	1720	1720
WR major elements (wt. %)												
SiO_2	74.21	74.23	74.13	74.13	74.15	74.64	74.38	74.55	74.25	74.45	74.26	74.18
TiO_2	0.28	0.28	0.29	0.29	0.29	0.28	0.28	0.28	0.28	0.28	0.28	0.28
Al_2O_3	13.48	13.48	13.51	13.54	13.53	13.34	13.45	13.38	13.49	13.38	13.43	13.48
Fe_2O_3	2.51	2.51	2.57	2.55	2.52	2.41	2.43	2.43	2.46	2.44	2.46	2.46
MnO	0.095	0.093	0.103	0.096	0.100	0.090	0.094	0.092	0.093	0.093	0.095	0.094
MgO	0.34	0.34	0.33	0.34	0.33	0.30	0.31	0.31	0.32	0.31	0.32	0.33
CaO	1.73	1.73	1.74	1.75	1.73	1.61	1.65	1.65	1.68	1.66	1.68	1.70
Na_2O	4.55	4.55	4.54	4.50	4.56	4.48	4.53	4.46	4.56	4.52	4.64	4.63
K_2O	2.76	2.74	2.74	2.75	2.74	2.78	2.83	2.80	2.82	2.79	2.79	2.78
P_2O_5	0.053	0.054	0.061	0.061	0.053	0.044	0.052	0.051	0.052	0.055	0.055	0.057
LOI	2.71	2.37	2.12	2.68	1.67	2.8	2.04	2.47	2.33	1.98	2.37	2.37
Total	99.56	99.57	99.48	99.48	99.58	99.4	99.2	99.4	99.47	99.51	100.13	99.78
WR trace elements (ppm)												
Li	43.17		42.95	46.43		43.16	40.85	40.27		43.13		
Sc	11.3		11.5	11.8		11.5	11.4	11.6		12.0		
V	2		2	2		3	2	2		2		
Cr	2.0		4.6	2.1		2.1	1.9	3.5		1.4		
Ni	0.2		0.4	0.2		0.2	0.2	1.0		0.2		
Cu	1.6		1.1	1.1		1.6	1.6	1.3		3.2		
Zn	72		73	73		73	72	78		76		
Ga	16.9		16.5	17.0		17.3	16.8	17.2		17.6		
Rb	104.1		96.5	101.3		100.1	102.7	105.9		105.8		
Sr	173		167	174		156	164	163		166		
Y	34.7		33.2	33.7		34.0	34.3	34.3		35.8		
Zr	232		225	234		230	231	235		243		
Nb	9.7		8.4	9.7		8.6	12.6	12.9		13.4		
Cs	5.26		4.84	5.23		5.00	4.85	4.94		5.11		
Ba	637		624	619		622	621	639		655		
La	27.0		25.8	26.2		26.1	25.9	26.9		27.4		
Ce	58.2		55.8	56.1		56.4	55.0	57.9		59.5		
Pr	7.16		6.73	6.72		6.71	6.54	6.80		6.94		
Nd	27.1		26.7	26.9		26.3	26.1	26.7		26.9		
Sm	6.02		5.72	5.84		5.70	5.46	5.95		5.86		
Eu	1.38		1.34	1.34		1.28	1.26	1.29		1.36		
Gd	6.51		6.14	6.45		6.12	5.75	6.31		6.33		
Tb	0.96		0.89	0.91		0.90	0.87	0.95		0.94		
Dy	6.05		5.79	5.85		5.66	5.55	5.85		5.79		
Ho	1.26		1.19	1.21		1.21	1.16	1.25		1.24		
Er	3.60		3.47	3.63		3.53	3.55	3.66		3.62		
Tm	0.568		0.528	0.552		0.518	0.517	0.529		0.544		
Yb	3.81		3.52	3.58		3.66	3.40	3.59		3.55		
Lu	0.558		0.536	0.548		0.558	0.520	0.561		0.539		
Hf	6.32		5.97	6.21		6.21	5.99	6.26		6.20		
Pb	23.1		19.8	24.8		19.3	21.5	22.9		23.2		
Th	11.25		10.73	11.12		11.06	10.66	11.17		11.22		
U	2.60		2.42	2.38		2.50	2.38	2.53		2.52		
Rb/Sr	0.60		0.60	0.58		0.64	0.63	0.65		0.64		
Eu/Eu*	0.67		0.69	0.67		0.66	0.69	0.64		0.68		

Table DR1. continued

Unit	Y2	Y2	Y2	Y2	Y3	Y3	Y3	Y3	Y4	Y4-Y5	Y4-Y5	Y4-Y5
SG	3	3	3	3	3	3	3	3	3	3	3	3
Sample	P2278	P2280	P2282	P2285	P2293	P2294	P2295	P2296	P2141	P2226A	P2226B	P2226C
Age BP	1720	1720	1720	1720	1720	1720	1720	1720	1720	1720	1720	1720
WR major elements (wt. %)												
SiO_2	74.21	74.17	74.27	74.01	74.02	73.85	74.16	74.08	74.11	74.00	73.82	74.00
TiO_2	0.28	0.28	0.29	0.30	0.29	0.30	0.29	0.29	0.29	0.30	0.30	0.29
Al_2O_3	13.48	13.47	13.47	13.57	13.57	13.61	13.52	13.55	13.54	13.60	13.61	13.54
Fe_2O_3	2.43	2.45	2.44	2.55	2.51	2.58	2.47	2.49	2.49	2.55	2.59	2.54
MnO	0.093	0.093	0.093	0.093	0.094	0.096	0.094	0.094	0.095	0.097	0.095	0.098
MgO	0.31	0.33	0.32	0.36	0.34	0.36	0.33	0.33	0.32	0.34	0.36	0.34
CaO	1.70	1.70	1.67	1.75	1.74	1.81	1.73	1.73	1.72	1.75	1.80	1.74
Na_2O	4.64	4.68	4.61	4.58	4.63	4.59	4.58	4.60	4.60	4.57	4.63	4.63
K_2O	2.79	2.78	2.78	2.74	2.76	2.74	2.78	2.77	2.77	2.74	2.73	2.76
P_2O_5	0.057	0.056	0.050	0.052	0.056	0.059	0.054	0.057	0.055	0.056	0.055	0.058
LOI	2.7	2.22	2.67	2.92	2.88	3.19	2.99	3.14	1.55	2.23	0.96	0.5
Total	100.08	99.85	99.57	100.08	99.81	99.8	99.86	99.84	100.24	100.08	99.74	99.28
WR trace elements (ppm)												
Li	42.83				43.12				45.81	45.03		41.35
Sc	11.8				11.6				11.7	11.6		11.7
V	2				2				2	2		2
Cr	2.3				3.4				5.4	1.7		3.4
Ni	0.1				0.1				0.1	0.2		0.1
Cu	1.3				1.1				1.0	1.0		1.0
Zn	74				75				76	74		73
Ga	17.2				17.6				16.9	17.2		16.6
Rb	102.9				104.3				106.3	102.9		107.5
Sr	163				174				176	172		173
Y	35.4				34.9				36.3	35.0		35.3
Zr	232				232				243	235		240
Nb	12.6				4.0				11.6	8.8		11.5
Cs	4.92				4.08				5.21	4.94		5.37
Ba	624				611				655	628		671
La	26.9				25.9				27.7	26.7		27.7
Ce	58.2				55.7				59.4	57.9		58.2
Pr	6.68				6.55				7.12	6.86		7.30
Nd	27.3				26.7				28.5	27.0		27.9
Sm	6.10				5.90				6.07	5.87		6.00
Eu	1.28				1.33				1.47	1.37		1.43
Gd	6.52				5.93				6.33	6.58		6.35
Tb	0.96				0.94				0.91	0.96		0.94
Dy	5.89				5.88				5.98	5.79		6.04
Ho	1.25				1.24				1.25	1.24		1.27
Er	3.59				3.74				3.68	3.57		3.66
Tm	0.550				0.555				0.565	0.551		0.561
Yb	3.54				3.70				3.63	3.67		3.62
Lu	0.556				0.578				0.572	0.548		0.566
Hf	5.83				6.26				6.55	6.20		6.31
Pb	21.4				21.1				21.3	19.5		21.3
Th	10.77				10.95				10.93	11.20		11.36
U	2.50				2.53				2.42	2.54		2.58
Rb/Sr	0.63				0.60				0.60	0.60		0.62
Eu/Eu*	0.62				0.69				0.73	0.67		0.71

Table DR1. continued

Unit	Y5	Y5	Y5	Y5	Y5	Y5	Y7	Y7	Y7	Y7	Y7	Y7
SG	3	3	3	3	3	3	3	3	3	3	3	3
Sample	P2227	P2228	P2229	P2231	P2233	P368M	P2286	P2287	P2288	P2289	P2290	P2291
Age BP	1720	1720	1720	1720	1720	1720	1720	1720	1720	1720	1720	1720
WR major elements (wt. %)												
SiO_2	73.69	73.99	74.01	74.02	74.00	59.13	74.03	73.99	74.03	73.97	73.94	73.98
TiO_2	0.31	0.30	0.29	0.29	0.29	1.51	0.29	0.29	0.29	0.29	0.29	0.30
Al_2O_3	13.76	13.69	13.63	13.63	13.58	15.90	13.58	13.53	13.52	13.54	13.59	13.55
Fe_2O_3	2.62	2.53	2.55	2.53	2.53	8.84	2.50	2.55	2.52	2.51	2.51	2.56
MnO	0.099	0.094	0.095	0.096	0.096	0.190	0.095	0.095	0.093	0.096	0.094	0.094
MgO	0.36	0.33	0.33	0.34	0.34	2.54	0.33	0.35	0.33	0.35	0.34	0.36
CaO	1.82	1.74	1.73	1.71	1.76	5.92	1.73	1.74	1.73	1.75	1.78	1.77
Na_2O	4.55	4.51	4.55	4.55	4.59	4.00	4.56	4.59	4.62	4.62	4.59	4.53
K_2O	2.74	2.76	2.76	2.77	2.76	1.26	2.83	2.80	2.80	2.81	2.80	2.79
P_2O_5	0.060	0.063	0.060	0.059	0.058	0.710	0.056	0.061	0.059	0.059	0.059	0.063
LOI	2.41	2.49	2.22	2.39	2.24	0.99	3.77	3.29	3.69	3.84	3.95	4.07
Total	99.38	99.88	99.67	99.38	100.09	99.02	99.13	99.79	100.01	99.56	100.12	100.11

WR trace elements (ppm)						
Li	40.52	39.47	38.94	35.83	38.28	
Sc	11.2	11.7	10.9	11.7	11.5	
V	2	2	2	3	2	
Cr	2.6	2.7	1.1	16.5	5.5	
Ni	0.2	0.2	0.2	0.2	0.3	
Cu	1.2	0.9	1.2	1.4	1.0	
Zn	73	75	70	74	74	
Ga	16.9	17.4	16.1	16.7	17.0	
Rb	101.2	103.3	97.9	101.1	100.3	
Sr	168	172	160	168	167	
Y	34.0	35.1	32.6	33.7	33.4	
Zr	228	234	215	223	226	
Nb	5.0	3.5	7.9	12.5	4.8	
Cs	4.02	4.11	3.82	4.84	4.05	
Ba	598	618	561	615	593	
La	24.8	26.5	24.2	26.1	25.8	
Ce	54.5	56.1	51.3	55.3	54.6	
Pr	6.62	6.61	6.11	6.70	6.41	
Nd	26.1	26.6	24.3	26.4	25.6	
Sm	5.62	5.85	5.45	5.58	5.75	
Eu	1.22	1.28	1.22	1.35	1.34	
Gd	5.66	5.76	5.38	5.92	5.91	
Tb	0.89	0.89	0.84	0.91	0.91	
Dy	5.72	5.89	5.43	5.75	5.80	
Ho	1.16	1.21	1.14	1.19	1.20	
Er	3.54	3.67	3.44	3.48	3.52	
Tm	0.537	0.560	0.526	0.534	0.529	
Yb	3.50	3.73	3.46	3.42	3.49	
Lu	0.550	0.591	0.539	0.524	0.557	
Hf	6.08	6.41	5.78	6.02	5.98	
Pb	21.1	22.0	19.7	22.4	20.8	
Th	10.75	10.96	10.16	10.81	10.48	
U	2.47	2.52	2.31	2.36	2.43	
Rb/Sr	0.60	0.60	0.61	0.60	0.60	
Eu/Eu*	0.66	0.68	0.69	0.72	0.70	

Table DR1. continued

Unit	Y7	Z	Z	Z
SG	3	3	3	3
Sample	P2292	P2173A	P2173B	P2260
Age BP	1720	~1700	~1700	~1700
WR major elements (wt. %)				
SiO_2	73.95	73.53	73.49	73.36
TiO_2	0.29	0.32	0.32	0.37
Al_2O_3	13.58	13.67	13.71	13.57
Fe_2O_3	2.51	2.67	2.68	2.92
MnO	0.095	0.099	0.097	0.101
MgO	0.35	0.39	0.40	0.41
CaO	1.74	1.87	1.86	1.89
Na_2O	4.62	4.62	4.64	4.59
K_2O	2.81	2.75	2.73	2.71
P_2O_5	0.058	0.080	0.075	0.074
LOI	3.66	0.82	0.87	0.87
Total	99.26	99.49	99.74	100.12
WR trace elements (ppm)				
Li		33.74	31.94	
Sc		11.7	11.2	
V		4	3	
Cr		4.6	6.3	
Ni		0.3	0.4	
Cu		1.2	1.3	
Zn		74	71	
Ga		16.6	16.3	
Rb		94.2	89.5	
Sr		163	159	
Y		31.5	30.9	
Zr		209	207	
Nb		7.9	7.9	
Cs		4.91	4.63	
Ba		578	557	
La		24.0	23.7	
Ce		52.4	51.0	
Pr		6.30	6.14	
Nd		24.6	23.6	
Sm		5.36	5.10	
Eu		1.31	1.22	
Gd		5.94	5.58	
Tb		0.87	0.82	
Dy		5.36	5.11	
Ho		1.13	1.08	
Er		3.30	3.19	
Tm		0.505	0.480	
Yb		3.32	3.10	
Lu		0.500	0.483	
Hf		5.56	5.43	
Pb		16.0	15.1	
Th		9.84	9.50	
U		2.20	2.16	
Rb/Sr		0.58	0.56	
Eu/Eu*		0.71	0.70	

Table DR2. Major and trace element compositions of groundmass (GM) glass and major element compositional range of melt inclusions (MI) from the final SG2 eruptions (U, V and W) and the SG3 eruptions (X,Y and Z) and subunits

Unit	**U**		**V**		**W**		**X**
Sample	P2151		P2161A		P2155B		P2157A
Type	GM glass	MI glass	GM glass	MI glass	GM glass	MI glass	GM glass
Glass major elements (wt. %)							
SiO_2	76.54 ±0.47	75.26-77.09	76.57 ±0.62	75.41-77.70	77.23 ±0.52	75.92-78.23	74.90 ±0.55
TiO_2	0.19 ±0.03	0.16-0.22	0.17 ±0.03	0.14-0.34	0.17 ±0.03	0.14-0.21	0.25±0.04
Al_2O_3	12.84 ±0.20	12.67-13.52	12.62 ±0.19	12.47-13.37	12.75 ±0.38	12.56-13.59	13.39 ±0.20
FeO	1.89 ±0.33	1.79-2.78	1.92 ±0.41	1.65-2.44	1.79 ±0.30	1.62-2.40	2.27 ±0.40
MnO	0.03 ±0.08	0-0.09	0.08 ±0.07	0.05-0.14	0.07 ±0.07	0.04-0.16	0.10±0.04
MgO	0.14 ±0.03	0.05-0.21	0.10 ±0.05	0.09-0.25	0.10 ±0.04	0.06-0.17	0.23 ±0.03
CaO	1.15 ±0.06	1.00-1.44	1.06 ±0.11	0.96-1.28	1.07 ±0.18	0.96-1.41	1.50 ±0.09
Na_2O	4.00 ±0.24	3.41-4.23	4.26 ±0.22	3.49-4.15	3.61 ±0.14	2.87-3.62	4.37 ±0.21
K_2O	3.05 ±0.13	2.83-3.19	3.07 ±0.15	2.68-3.04	3.02 ±0.14	2.72-3.08	2.83 ±0.12
Cl	0.16 ±0.03	0.16-0.21	0.15 ±0.03	0.11-0.20	0.16 ±0.02	0.16-0.19	0.16 ±0.02
Total	99.6	94.1-100.9	100.1	94.6-97.9	98.5	93.1-98.7	100.6
n	23	21	23	15	14	16	18
Glass trace elements (ppm)							
Li	41.26		38.86		38.59		40.55
Sc	10.2		10.5		10.4		11.2
V	0		0		1		1
Cr	0.1		0.5		0.3		0.3
Ni	bdl		0.0		0.1		bdl
Cu	2.9		2.6		4.3		3.5
Zn	63		64		63		68
Ga	15.3		16.3		15.7		16.3
Rb	107.4		112.3		112.4		104.8
Sr	105		104		112		151
Y	34.0		36.9		35.9		36.1
Zr	215		224		219		244
Nb	7.9		2.1		8.7		2.8
Cs	5.26		5.52		5.39		5.10
Ba	637		698		681		713
La	25.9		28.1		27.5		27.3
Ce	56.6		60.2		58.9		59.2
Pr	6.59		7.25		7.22		7.15
Nd	26.2		28.4		28.2		27.0
Sm	5.66		6.10		5.93		5.99
Eu	1.11		1.19		1.21		1.29
Gd	5.59		6.39		6.16		6.28
Tb	0.89		0.97		0.95		0.93
Dy	5.59		6.19		6.16		6.01
Ho	1.21		1.31		1.27		1.25
Er	3.61		3.89		3.77		3.82
Tm	0.534		0.557		0.554		0.559
Yb	3.66		3.95		3.73		3.81
Lu	0.549		0.588		0.580		0.588
Hf	5.95		6.18		6.15		6.28
Pb	21.1		22.1		22.1		22.0
Th	10.90		11.52		11.21		10.79
U	2.43		2.63		2.67		2.60
Rb/Sr	1.02		1.08		1.01		0.69
Eu/Eu*	0.60		0.58		0.61		0.65
Temp	816 ˚C		813 ˚C		813 ˚C		849 ˚C
log **η**	5.17		5.17		5.32		4.72

Oxide abundances normalised to 100 % on a volatile free basis, with original analytical totals given. Major elements measured by Electron Probe Micro-Analysis (EPMA), trace elements measured by solution-ICPMS for pure groundmass glass separates only. Temperatures are averages from Barker et al. (2015) using the orthopyroxene-liquid thermometer of Putirka (2008). Viscocity (log η) of melt (in *Pa s*) calculated using the model of Giordano et al. (2008) assuming 4.5 wt. % H_2O content. Other details as in Table DR1. See Barker et al. (2015) for analytical methods and standards.

Table DR2. continued

Unit		Y1		Y3		Y7		Z
Sample		P2119		P2296		P2287		P2173A
Type	MI glass	GM glass	MI glass	GM glass	MI glass	GM glass	MI glass	GM glass
Glass major elements (wt. %)								
SiO_2	75.34-76.93	74.80 ±0.62	74.18-76.17	75.03 ±0.55	74.71-77.00	75.24 ±0.30	75.17-76.83	76.80 ±0.63
TiO_2	0.16-0.26	0.23±0.04	0.18-0.40	0.24±0.05	0.19-0.28	0.25±0.02	0.21-0.32	0.24±0.03
Al_2O_3	12.85-13.49	13.34 ±0.30	12.66-13.95	13.44 ±0.24	12.61-13.50	13.33 ±0.29	12.55-13.84	12.46 ±0.22
FeO	1.63-2.94	2.35 ±0.55	1.95-2.91	2.27 ±0.34	1.84-2.98	2.23 ±0.55	1.63-2.93	2.34 ±0.33
MnO	0.03-0.14	0.10±0.07	0.02-0.17	0.11±0.06	0.07-0.19	0.10±0.06	0.04-0.17	0.08±0.08
MgO	0.15-0.26	0.25 ±0.02	0.20-0.32	0.22 ±0.09	0.15-0.27	0.24 ±0.04	0.05-0.24	0.16 ±0.04
CaO	1.23-1.53	1.50 ±0.06	1.37-1.62	1.52 ±0.13	1.14-1.72	1.49 ±0.15	1.34-1.60	1.11 ±0.07
Na_2O	3.52-4.31	4.49 ±0.22	3.77-4.16	4.26 ±0.48	3.34-4.48	4.13 ±0.22	3.54-4.07	4.25 ±0.34
K_2O	2.55-2.83	2.77 ±0.20	2.59-2.85	2.75 ±0.11	2.35-2.90	2.81 ±0.18	2.52-2.93	3.02 ±0.12
Cl	0.12-0.17	0.16 ±0.03	0.13-0.20	0.15 ±0.03	0.14-0.19	0.18 ±0.03	0.15-0.21	0.16 ±0.03
Total	94.0-99.7	100.4	93.9-96.9	100.13	94.2-100.2	98	94.5-96.4	98.7
n	12	8	14	11	21	10	28	17
Glass trace elements (ppm)								
Li		44.84		42.56		36.66		42.45
Sc		10.6		10.8		10.6		10.8
V		1		1		1		2
Cr		0.3		0.4		1.2		0.2
Ni		0.1		0.1		0.1		0.0
Cu		5.2		2.4		2.0		1.9
Zn		71		69		68		68
Ga		16.3		16.2		15.6		15.6
Rb		105.2		101.1		93.9		104.6
Sr		148		152		145		131
Y		35.0		34.3		32.6		35.1
Zr		238		231		217		238
Nb		3.9		5.5		4.4		5.3
Cs		5.77		5.64		5.29		5.70
Ba		661		644		614		651
La		27.4		26.7		25.2		27.1
Ce		59.5		57.8		54.4		58.5
Pr		6.91		6.74		6.48		6.76
Nd		27.4		26.7		25.3		27.1
Sm		5.96		5.86		5.45		5.80
Eu		1.25		1.34		1.23		1.23
Gd		6.13		6.06		5.66		6.10
Tb		0.98		0.94		0.86		0.93
Dy		6.07		5.96		5.46		5.96
Ho		1.27		1.23		1.14		1.25
Er		3.82		3.73		3.42		3.76
Tm		0.585		0.550		0.517		0.565
Yb		3.75		3.71		3.38		3.72
Lu		0.591		0.571		0.513		0.577
Hf		6.59		6.30		5.74		6.42
Pb		21.9		21.7		19.4		21.5
Th		11.12		11.05		9.91		11.07
U		2.62		2.52		2.28		2.52
Rb/Sr		0.71		0.67		0.65		0.79
Eu/Eu*		0.63		0.69		0.68		0.63
Temp		851 ˚C		852 ˚C		853 ˚C		853 ˚C
Viscocity		4.67		4.73		4.76		4.78

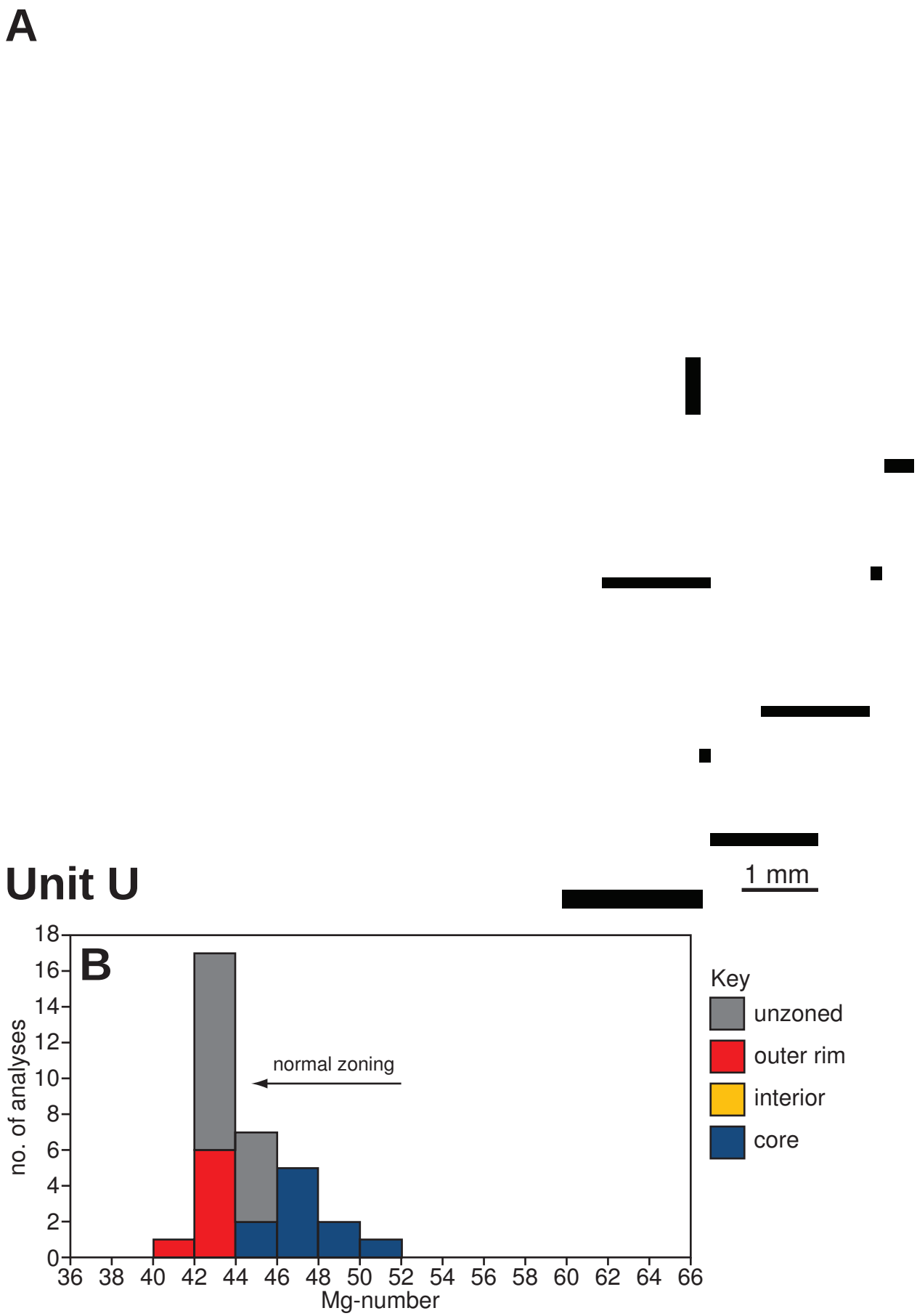

Fig. DR1. (A) Orthopyroxene textures from Unit U (SG2) in plain light photograph (left) and corresponding Back-Scattered Electron (BSE) images (right). Dark shades in BSE zoning are relatively low FeO or high MgO, light shades are high FeO or low MgO **(B)** Histogram showing orthopyroxene compositions for zones within single crystals from **A**, analysed by EPMA. Mg-number is calculated as Mg= 100*Mg/Mg+Fe_{total} (modified from Barker et al., 2015)

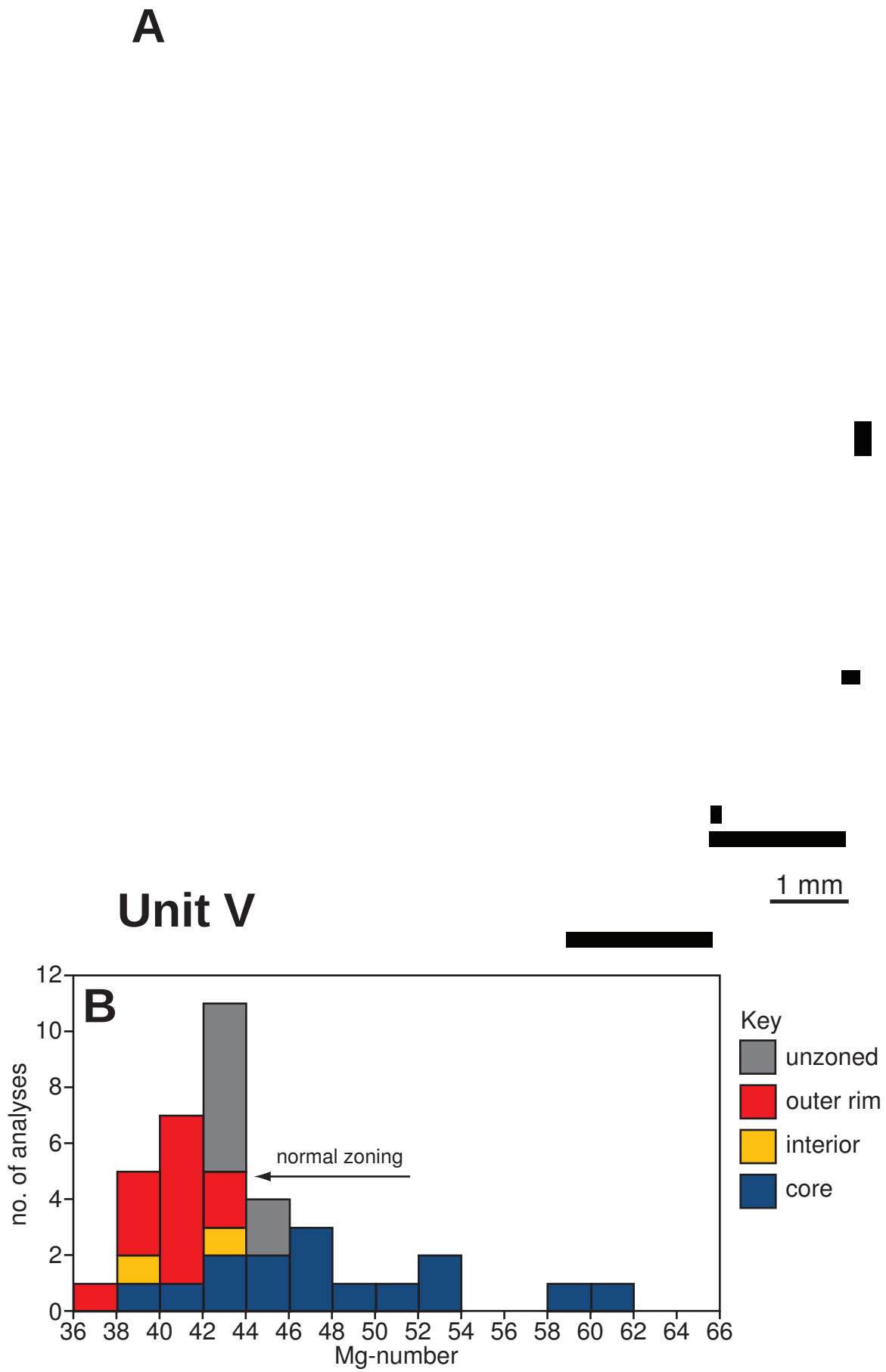

Fig. DR2. (A) Orthopyroxene textures from Unit V (SG2) in plain light photograph (left) and corresponding BSE images (right). **(B)** Histogram showing orthopyroxene compositions for zones within single crystals from **A**, analysed by EPMA. Other details as in Fig. DR1.

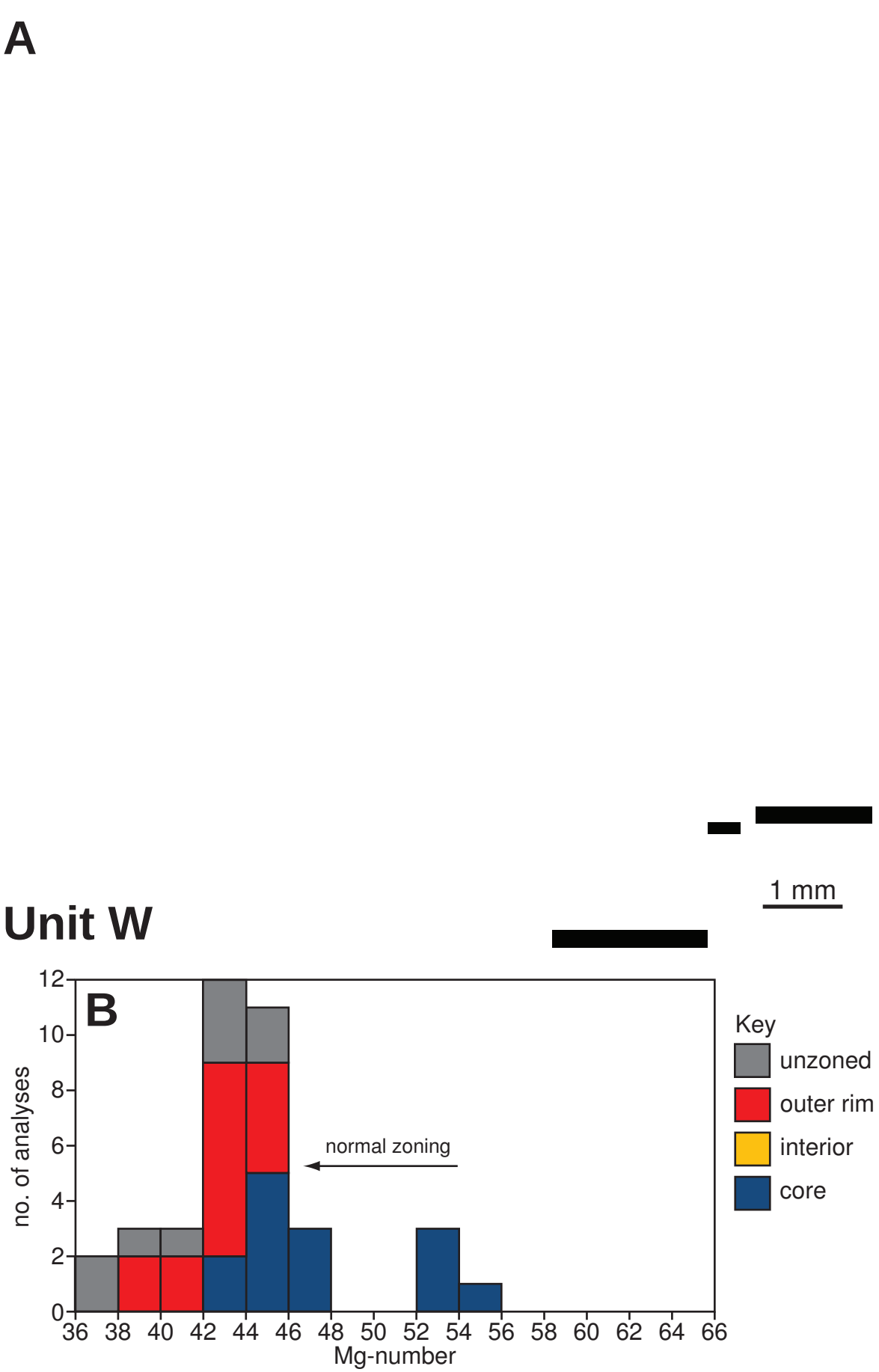

Fig. DR3. (A) Orthopyroxene textures from Unit W (SG2) in plain light photograph (left) and corresponding BSE images (right). **(B)** Histogram showing orthopyroxene compositions for zones within single crystals from **A**, analysed by EPMA. Other details as in Fig. DR1.

A

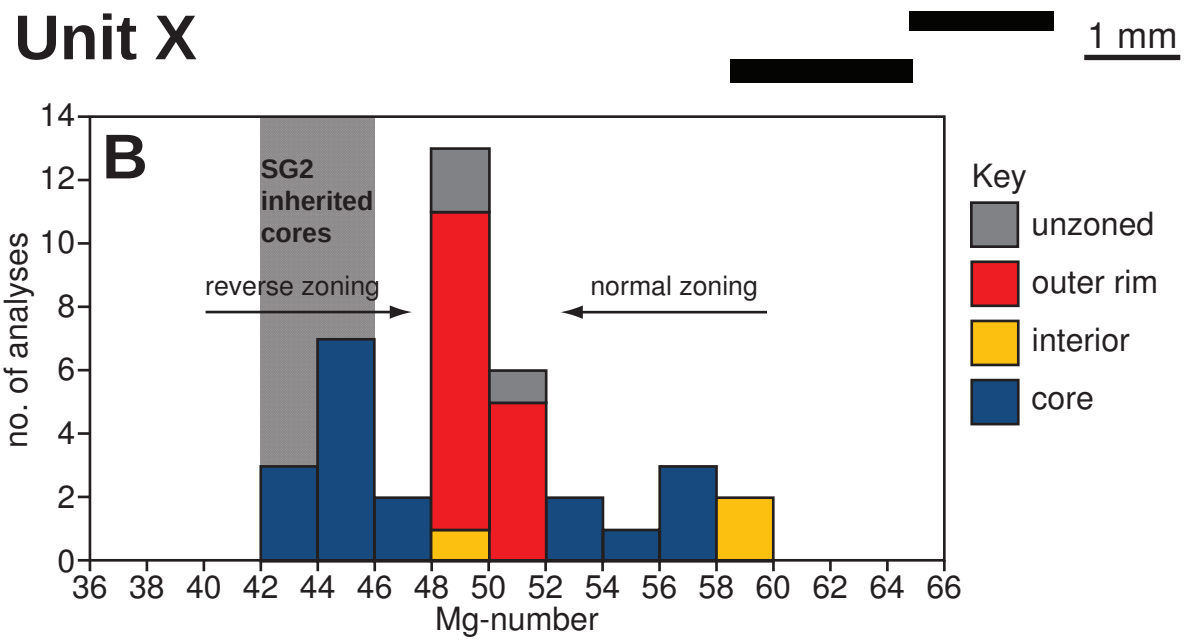

Fig. DR4. (A) Orthopyroxene textures from Unit X (SG3) in plain light photograph (left) and corresponding BSE images (right). **(B)** Histogram showing orthopyroxene compositions for zones within single crystals from **A**, analysed by EPMA. Cross-hatched area refers to dominant compositional mode for SG2 orthopyroxenes from Figs DR1-DR3. Other details as in Fig. DR1.

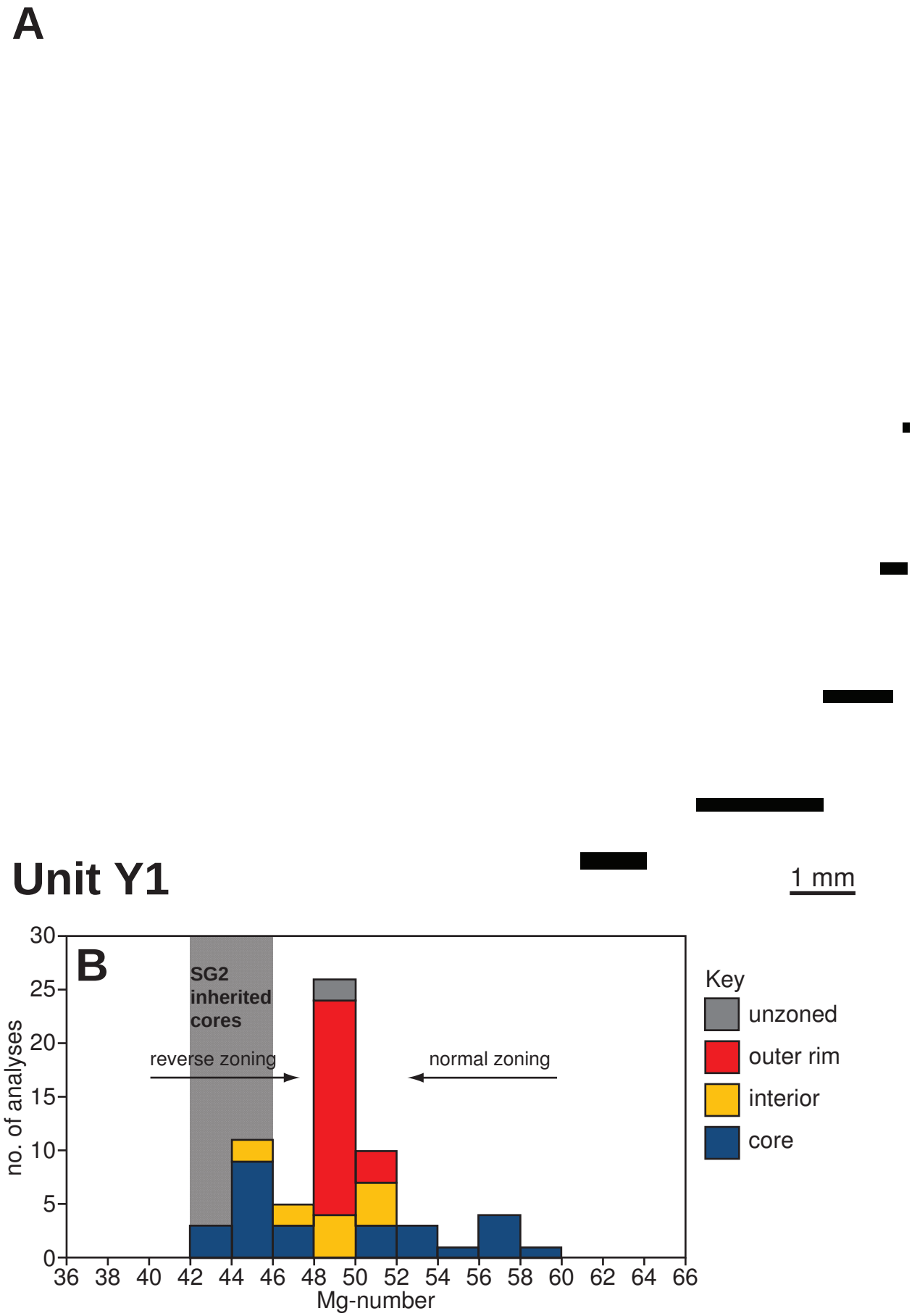

Fig. DR5. (A) Orthopyroxene textures from Unit Y1 (SG3) in plain light photograph (left) and corresponding BSE images (right). **(B)** Histogram showing orthopyroxene compositions for zones within single crystals from **A**, analysed by EPMA. Cross-hatched area refers to dominant compositional mode for SG2 orthopyroxenes from Figs DR1-DR3. Other details as in Fig. DR1.

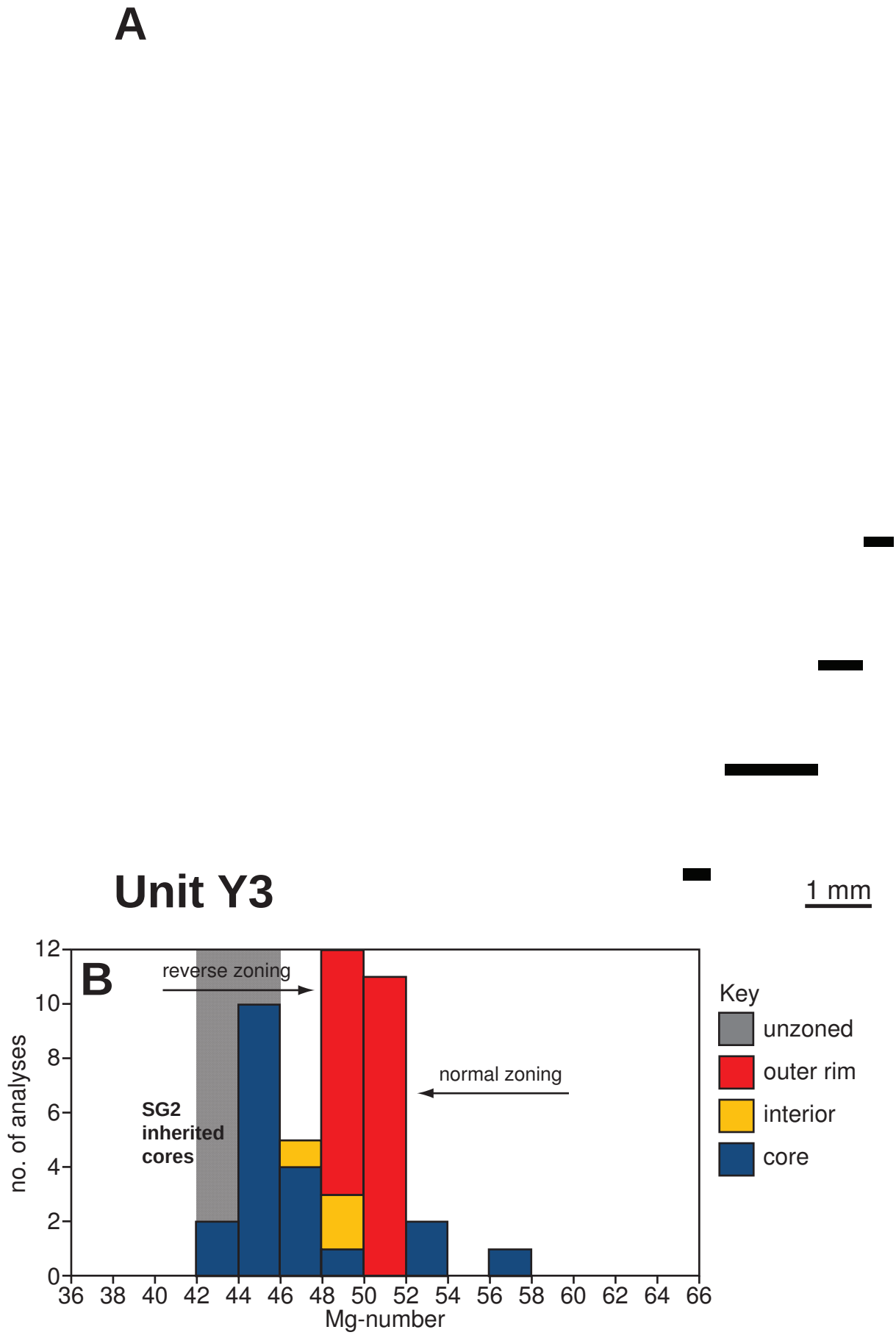

Fig. DR6. (A) Orthopyroxene textures from Unit Y3 (SG3) in plain light photograph (left) and corresponding BSE images (right). **(B)** Histogram showing orthopyroxene compositions for zones within single crystals from **A**, analysed by EPMA. Cross-hatched area refers to dominant compositional mode for SG2 orthopyroxenes from Figs DR1-DR3. Other details as in Fig. DR1.

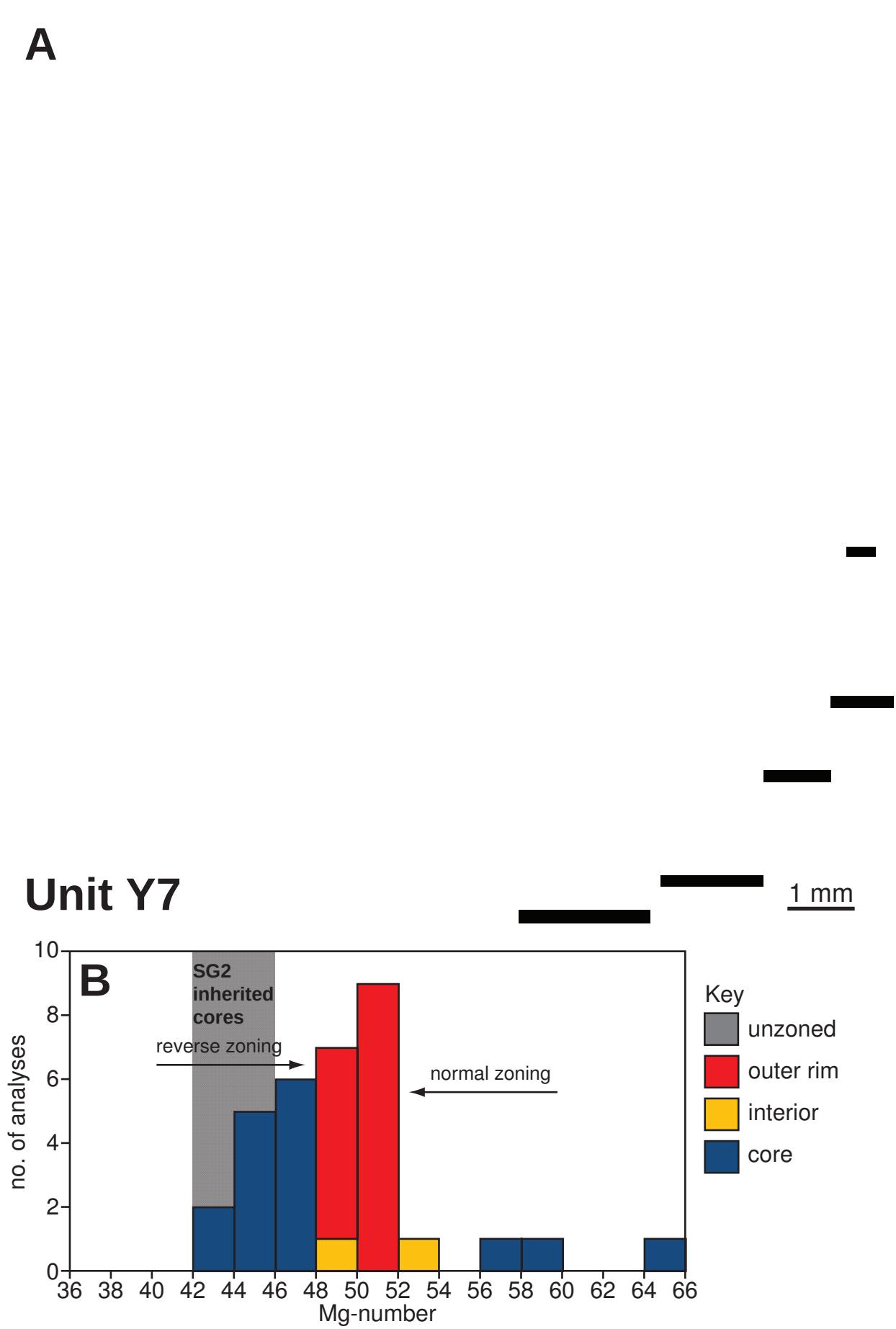

Fig. DR7. (A) Orthopyroxene textures from Unit Y7 (SG3) in plain light photograph (left) and corresponding BSE images (right). **(B)** Histogram showing orthopyroxene compositions for zones within single crystals from **A**, analysed by EPMA. Cross-hatched area refers to dominant compositional mode for SG2 orthopyroxenes from Figs DR1-DR3. Other details as in Fig. DR1.

A

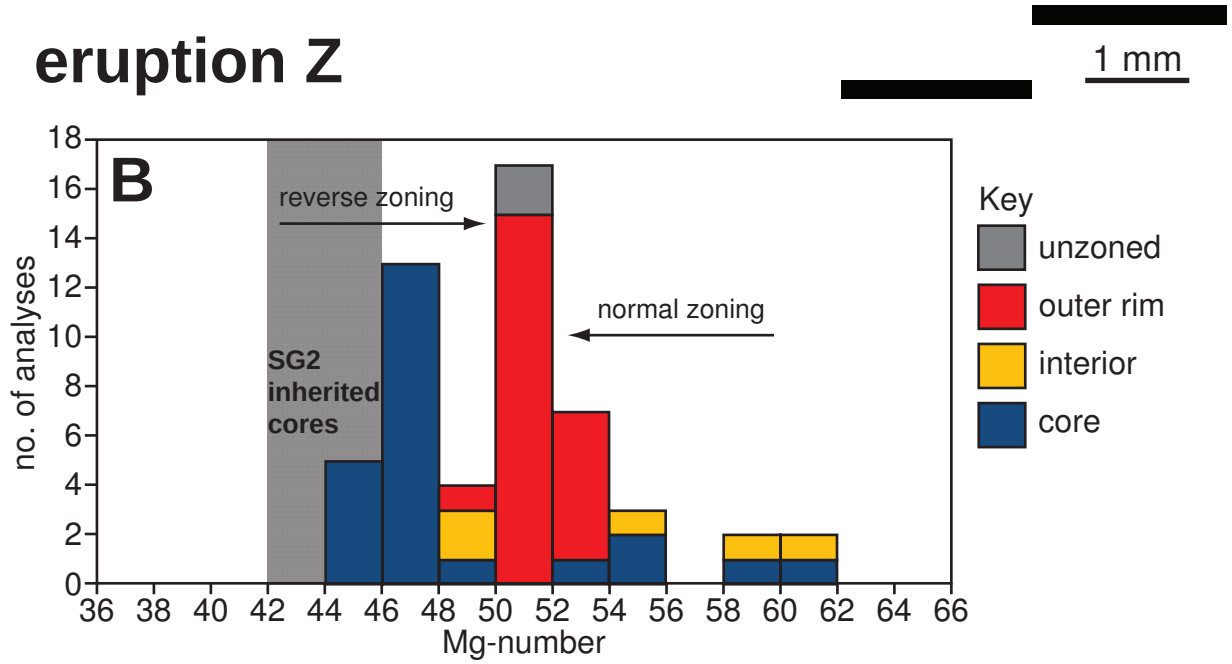

Fig. DR8. (A) Orthopyroxene textures from eruption Z (SG3) in plain light photograph (left) and corresponding BSE images (right). **(B)** Histogram showing orthopyroxene compositions for zones within single crystals from **A**, analysed by EPMA. Cross-hatched area refers to dominant compositional mode for SG2 orthopyroxenes from Figs DR1-DR3. Other details as in Fig. DR1.

Diffusion modelling in orthopyroxene

A strong negative linear relationship (R^2=0.95) has been observed between back-scattered electron (BSE) image greyscale values and the Mg/(Mg + Fe) content of orthopyroxene (Allan et al., 2013; Cooper, 2014; Chamberlain et al., 2014), and therefore the zoning observed in BSE images is inferred to be an accurate representation of the Fe-Mg content. This linear relationship allows compositional gradients in Fe and Mg concentrations to be investigated at a much higher spatial resolution than is possible from spot analyses alone (Morgan et al., 2004; Martin et al., 2008; Saunders et al., 2012; Allan et al., 2013). Diffusional geochronometry is used here to model the evolution of compositional profiles within zoned orthopyroxene crystals to determine the time elapsed since compositional variations were introduced. Typically, diffusion modelling assumes that the compositional boundaries initially had step-wise gradients, which over time at magmatic temperatures were modified by element diffusion to form sigmoidal shaped concentration gradients until quenching on eruption (e.g. Zellmer et al., 1999; Costa et al., 2003; Morgan et al., 2004, 2006; Costa and Dungan, 2005; Wark et al., 2007; Saunders et al., 2012; Allan et al., 2013). The initial compositional gradient is modelled forwards in time until it matches the observed profile and can be regarded as representing a maximum time, as the exact initial condition is not known.

In this study we use the methods of Allan et al. (2013) to calculate timescales of Fe-Mg diffusion in orthopyroxene. Image J (http://rsb.info.nih.gov/ij/) was used to extract spatially resolved profiles of BSE intensity across crystal zonation boundaries to quantify Mg/(Mg + ΣFe) profiles from rotated images. Fe-Mg profiles were obtained along the crystallographic a- or b-axis to avoid anisotropy effects, as growth effects have been observed along the c-axis of orthopyroxene (e.g. Allan et al. 2013; Figure DR9). Due to fO_2 dependence of $D_{Fe\text{-}Mg}$ in orthopyroxene (Ganguly and Tazzoli, 1994), the formula of Ganguly and Tazzoli (1994) modified as in Allan et al. (2013) is used to calculate $D_{Fe\text{-}Mg}$:

1

where X_{Fe} is the molar proportion of the Fe end member (ferrosilite), T is temperature in Kelvins, and fO_2 is oxygen fugacity. Finite-difference software was used to generate a database of simulated diffusion profiles, which obey composition-dependent diffusion under 1-D (linear) diffusion geometry, as detailed in Allan et al. (2013). This study adopts average

Figure DR9. Element maps of a representative orthopyroxene crystal from Unit Y showing the contrasts between fast diffusing (Mg) and slow diffusing (Ca+Al) elements and the relative preservation of initially sharp boundaries in a strongly zoned crystal. Light colours in WDS maps represent relatively high and dark colours are relatively low concentrations. Note the difference in zonation between the a-axis and c-axis directions, where the zoning parallel to the *c*-axis is smeared out and is kinematically controlled by a rapid growth regime, whereas sharp boundaries in slow-diffusing elements are largely preserved parallel to the *a*-axis with the slow-diffusing elements (Allan et al., 2013).

temperatures and fO_2 values calculated using mineral-mineral and mineral-melt equilibria for each eruptive unit from Barker et al. (2014). Oxygen fugacities were estimated using the Fe-Ti oxide equilibrium models of Ghiorso and Evans (2008) and Sauerzapf et al. (2008). For uncertainty calculations on single model-age determinations, conservative uncertainties of ±30 °C and ±0.3 ΔNNO log units for oxygen fugacity were used to generate inferred maximum and minimum timescales. Statistical analyses were also conducted across each profile, with the uncertainty on the greyscale profile essentially representing random thermal noise in the BSE detector. The plateaux at either end of a sigmoidal diffusion profile should be flat and profiles which had variation in the plateaux that exceeded the calculated 2 standard-error value, based on the number of averaged pixels were rejected. The relatively large width of the diffusion profiles investigated in this study (Figs DR10-14) means that common problems reported in other studies of convolution and pixel size were not considered to be of significant effect (Morgan et al., 2004; Cooper, 2014). A comprehensive summary of the measured and modelled Fe-Mg diffusion profiles across the crystal boundaries are presented in Figs DR10-14.

X1_OPX2_normal

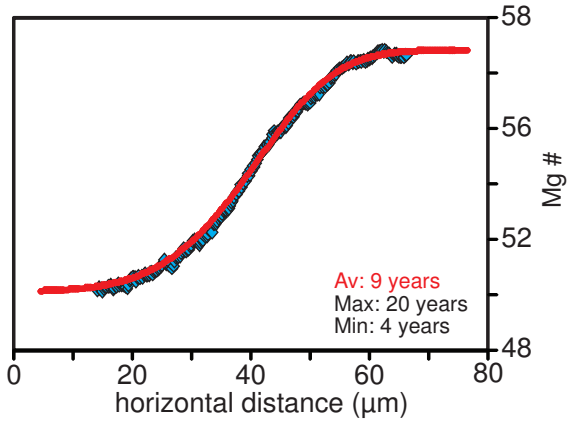

X1_OPX5_reverse

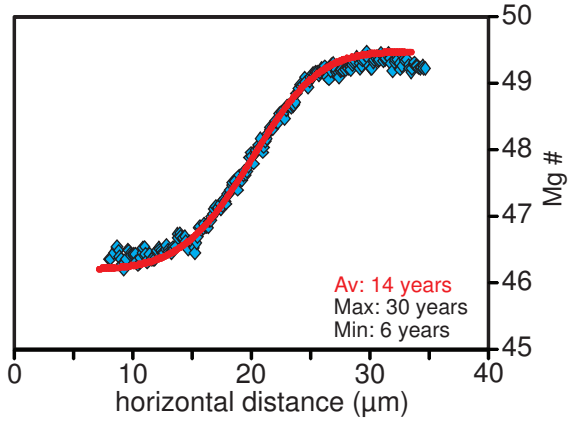

X1_OPX7_reverse

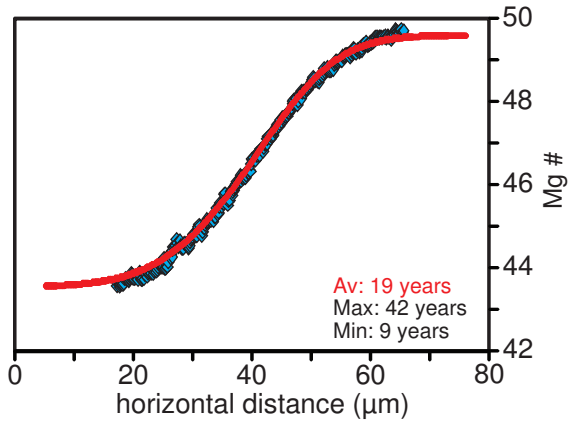

X1_OPX8_Profile1_reverse

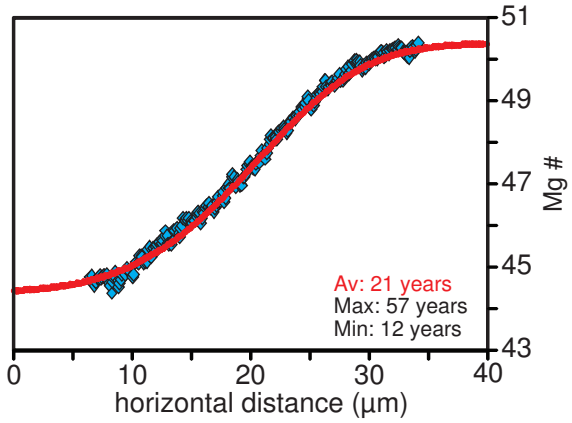

Fig. DR10. *Caption over page*

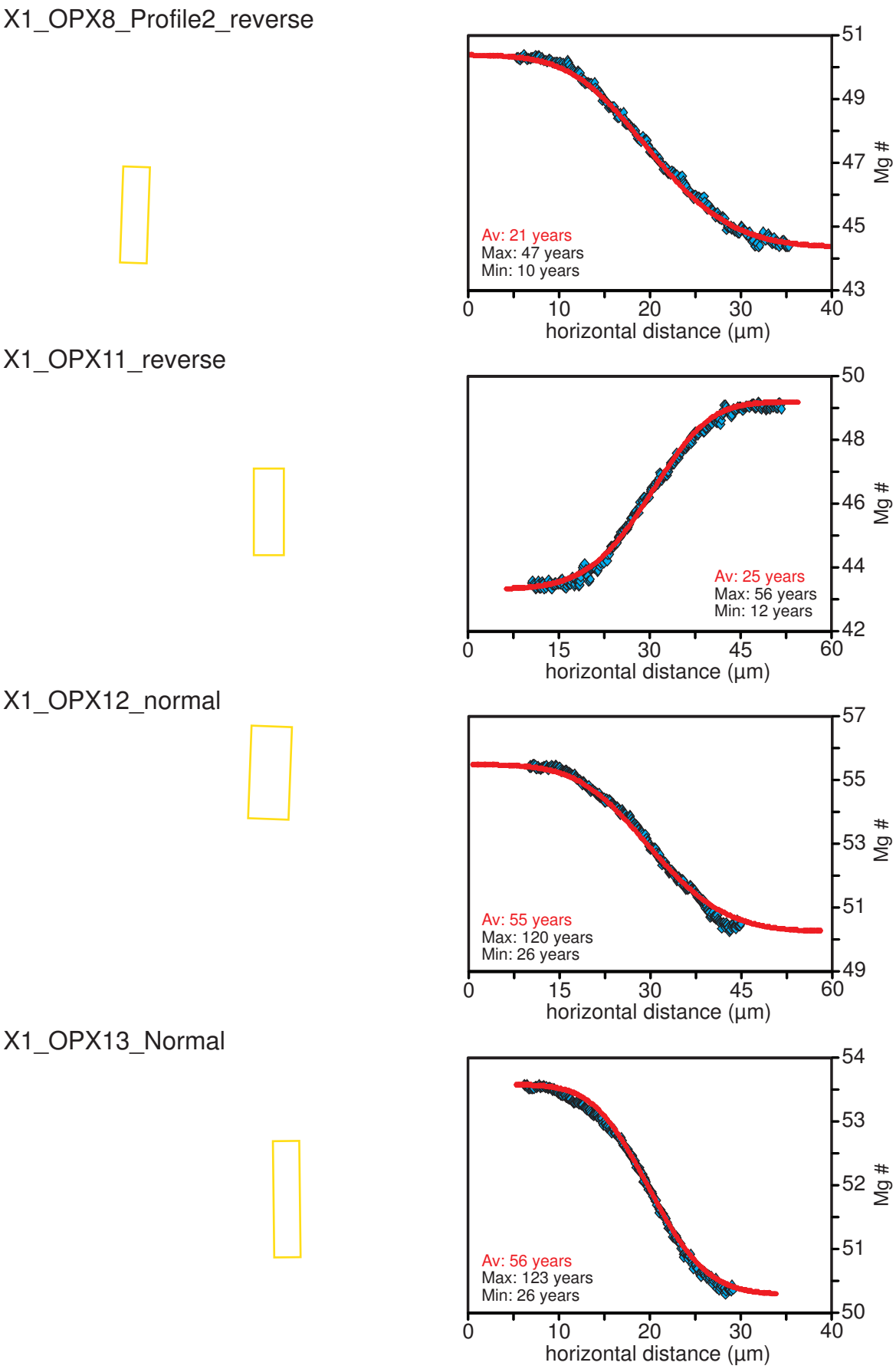

Fig. DR10. BSE images (left) and corresponding Fe-Mg diffusion models (right) of zoned orthopyroxene from Unit X. Yellow boxes in BSE images represent areas where diffusion modeling was undertaken. Red curves represent the modeled profile of an initially sharp compositional boundary and diamond symbols represent greyscale-calibrated Mg # (following Allan et al., 2013). Average (Av) diffusion model timescales given for parameter estimates of 860 °C, 1.5 MPa and log fO_2 of 0.2 ΔNNO from Barker et al. (2015). Maximum (Max) and minimum (Min) timescales use uncertainties ±30 ºC or ± 0.3 log units ΔNNO.

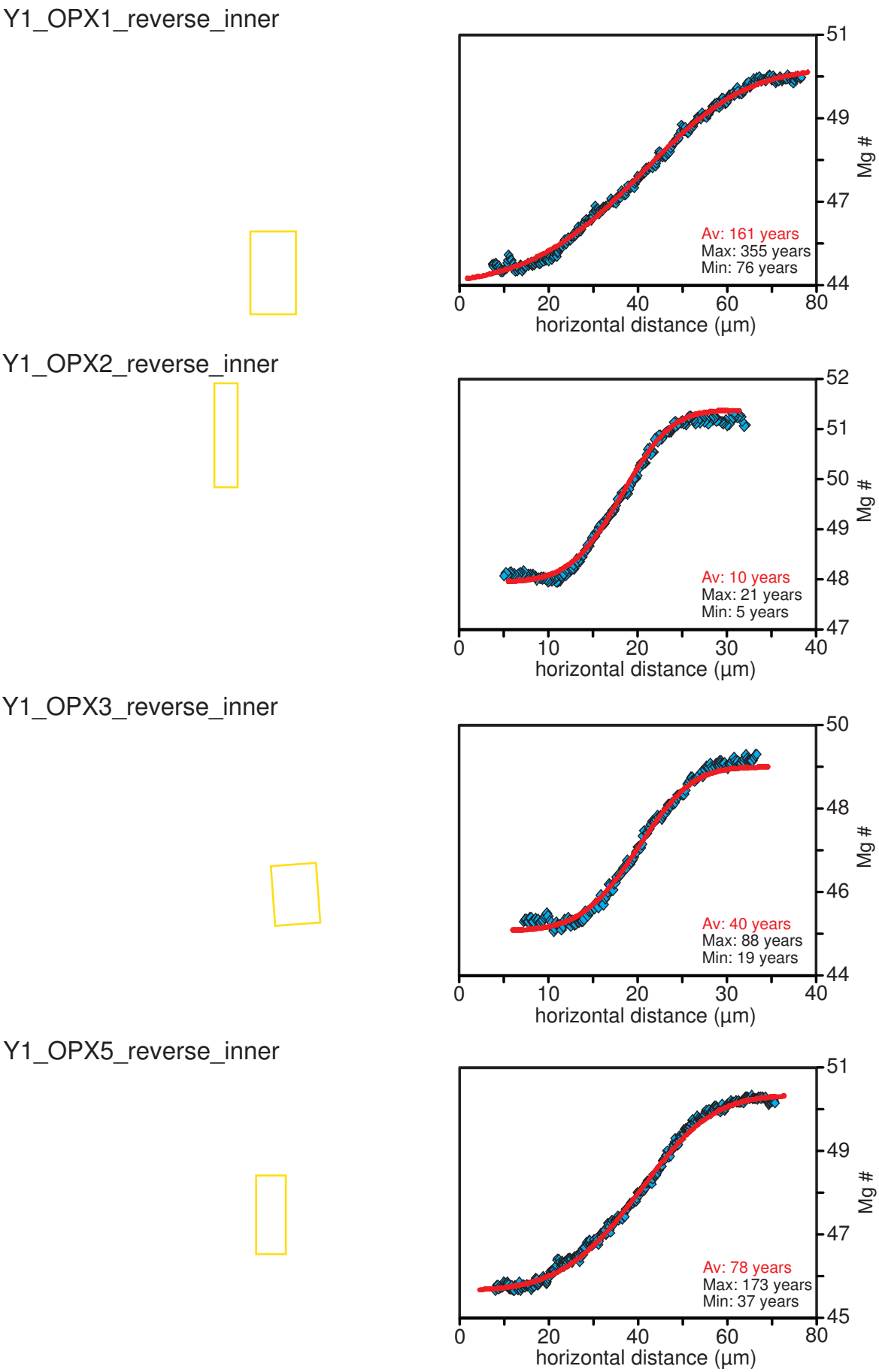

Fig. DR11. *Caption over page*

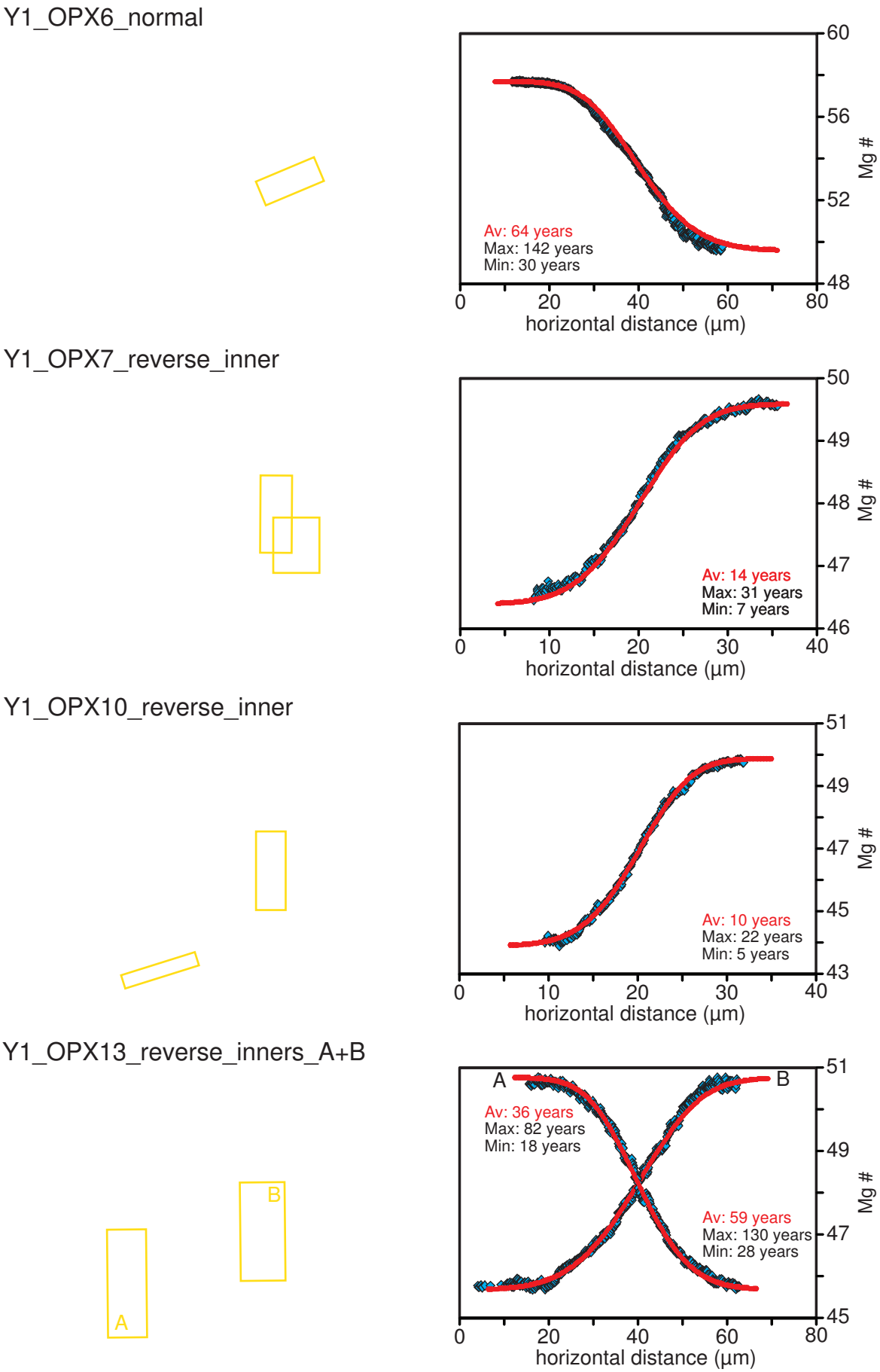

Fig. DR11. *Caption over page*

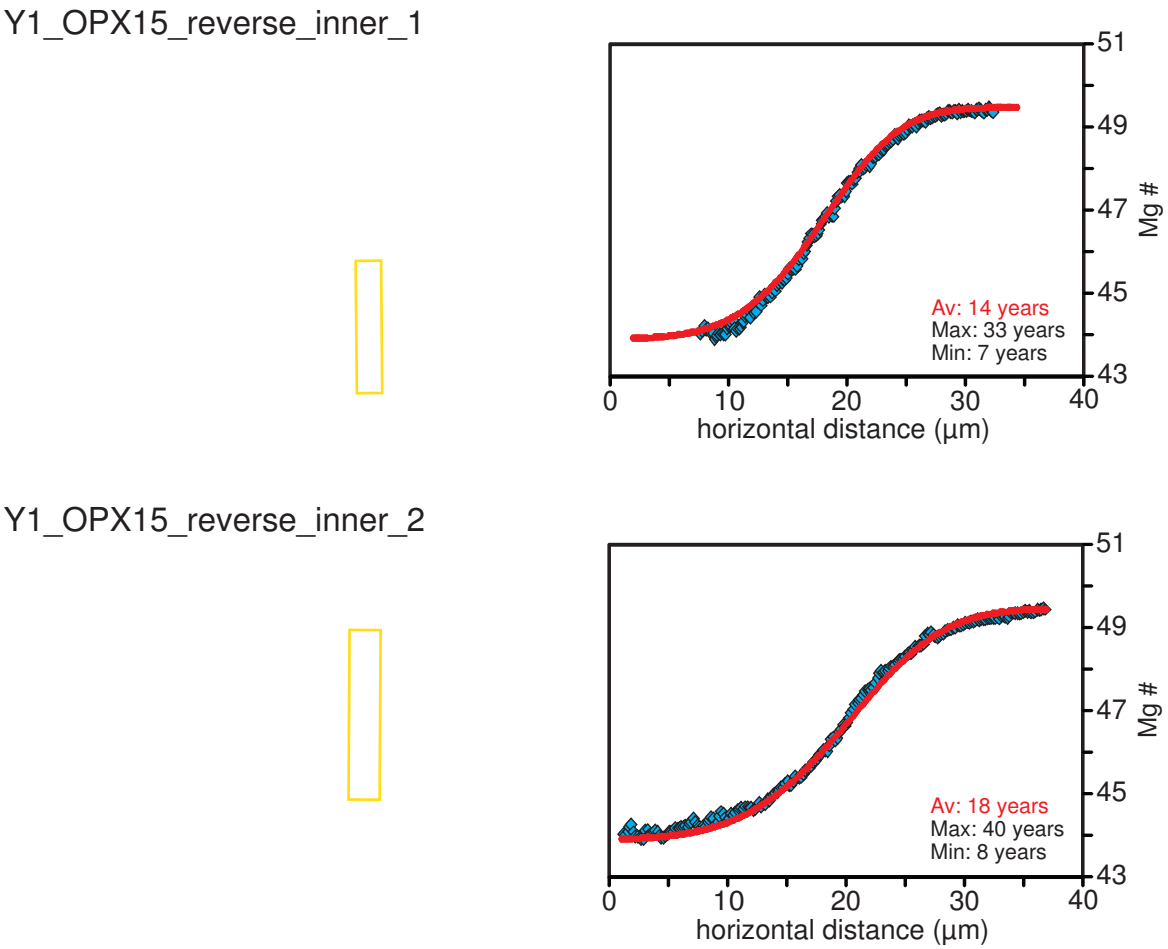

Fig. DR11. BSE images (left) and corresponding Fe-Mg diffusion models (right) of zoned orthopyroxene from Unit Y1. Average (Av) diffusion model timescales given for parameter estimates of 860 °C, 1.5 MPa and log fO_2 of 0.2 ΔNNO from Barker et al. (2015). Maximum (Max) and minimum (Min) timescales use uncertainties ±30 ºC or ± 0.3 log units Δ NNO. Other details as in Fig. DR10

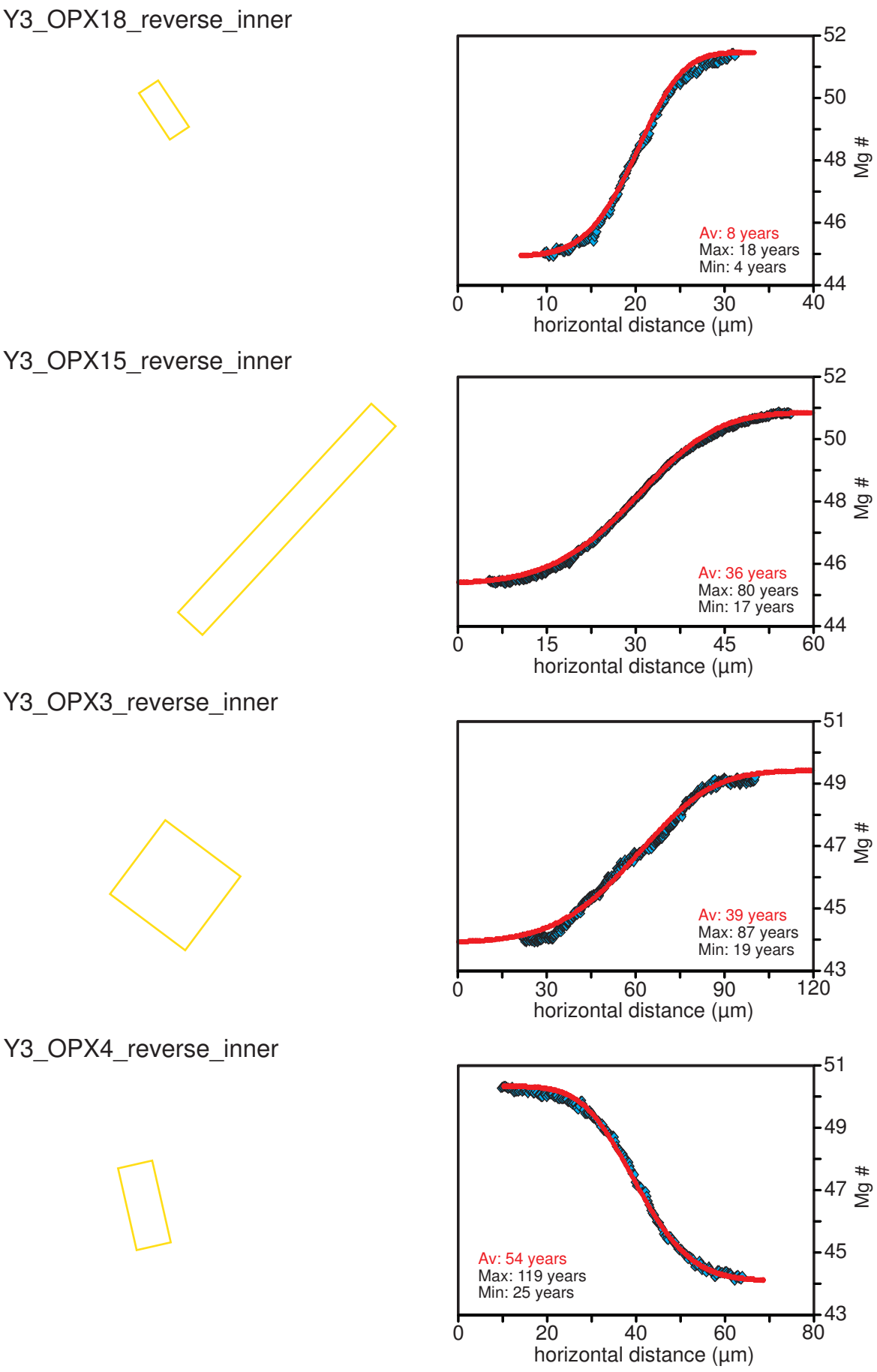

Fig. DR12. *Caption over page*

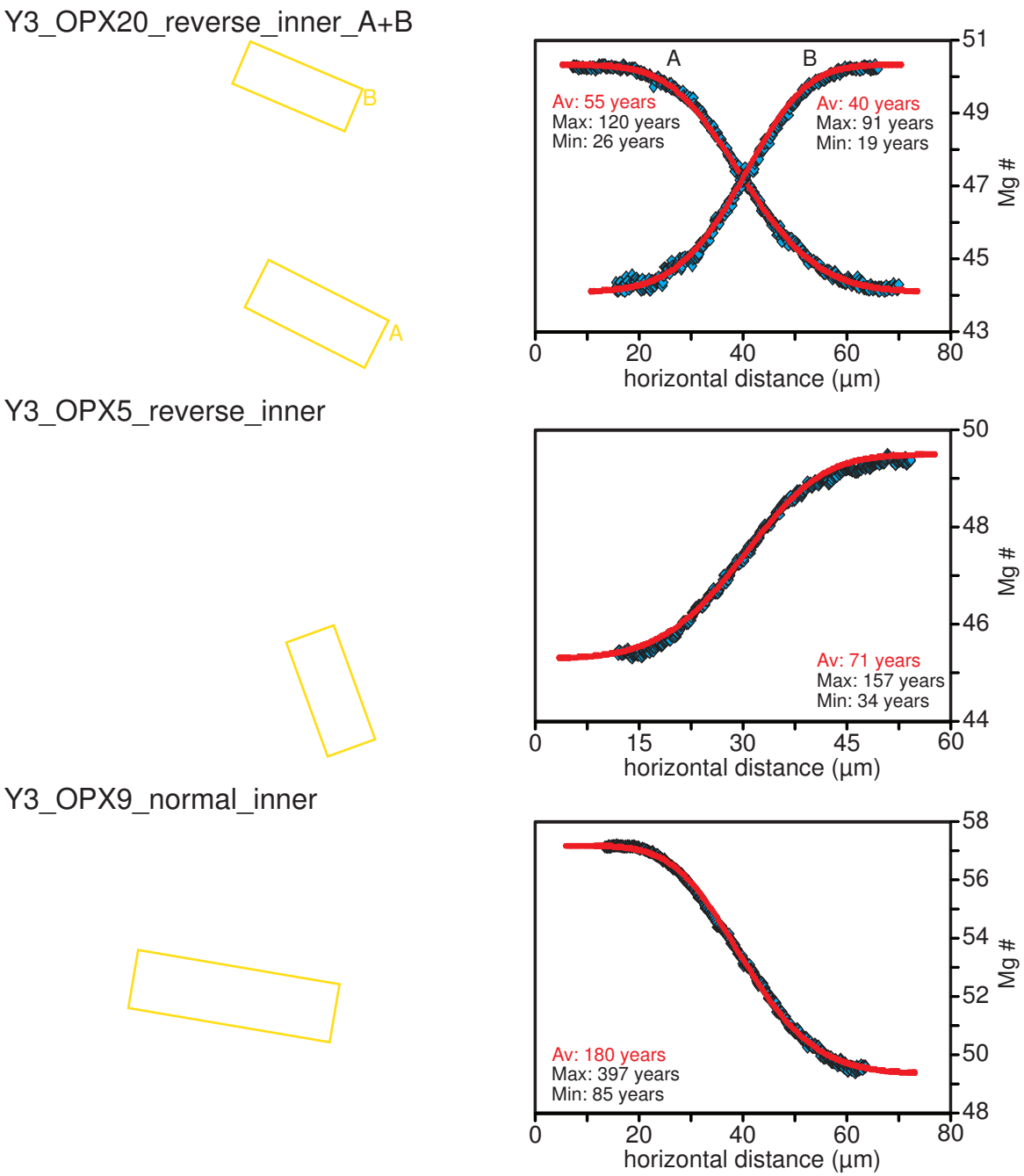

Fig. DR12. BSE images (left) and corresponding Fe-Mg diffusion models (right) of zoned orthopyroxene from Unit Y3. Average (Av) diffusion model timescales given for parameter estimates of 860 °C, 1.5 MPa and log fO_2 of 0.2 ΔNNO from Barker et al. (2015). Maximum (Max) and minimum (Min) timescales use uncertainties ±30 ºC or ± 0.3 log units Δ NNO. Other details as in Fig. DR10.

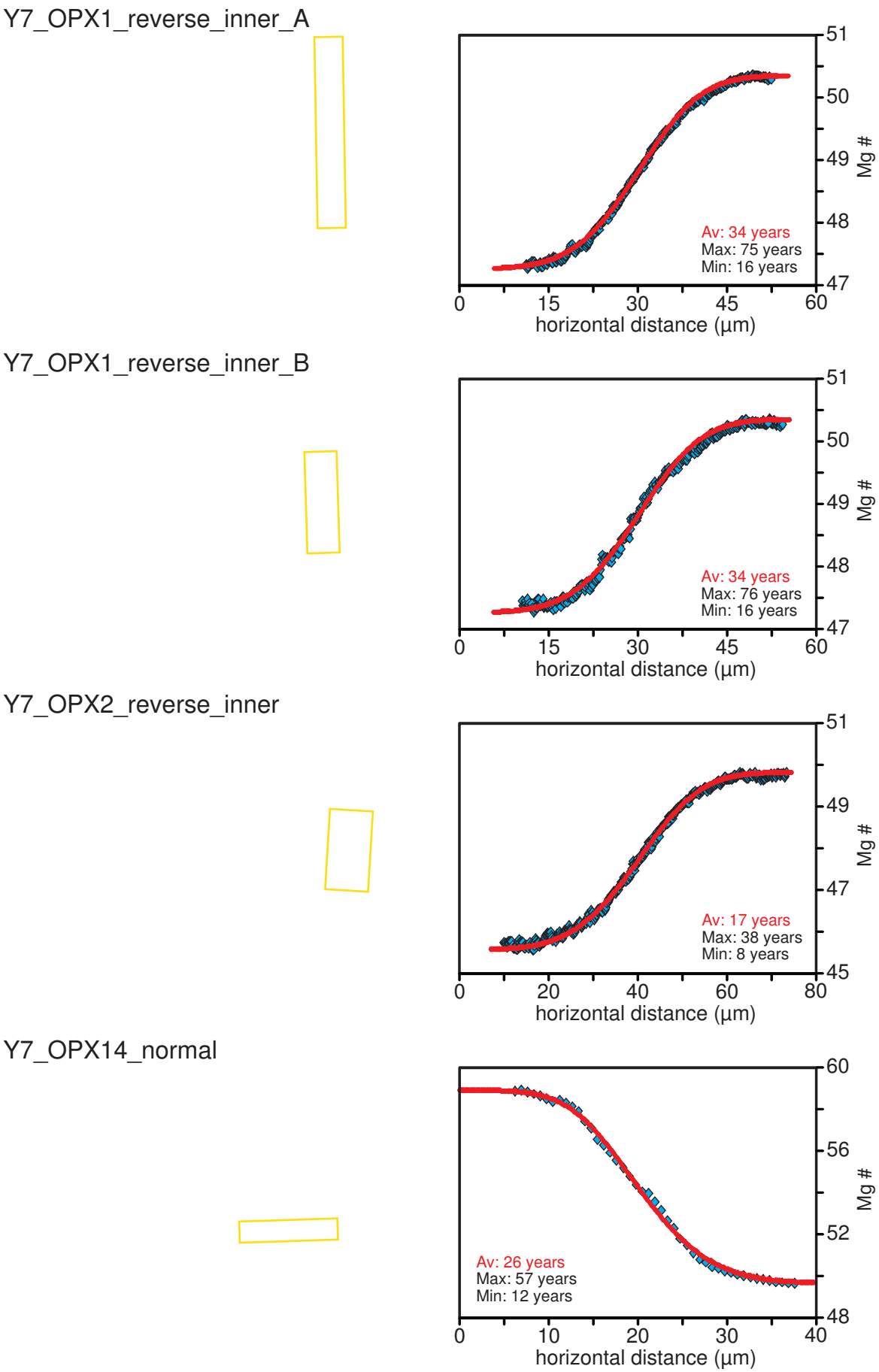

Fig. DR13. *Caption over page*

Y7_OPX13_reverse

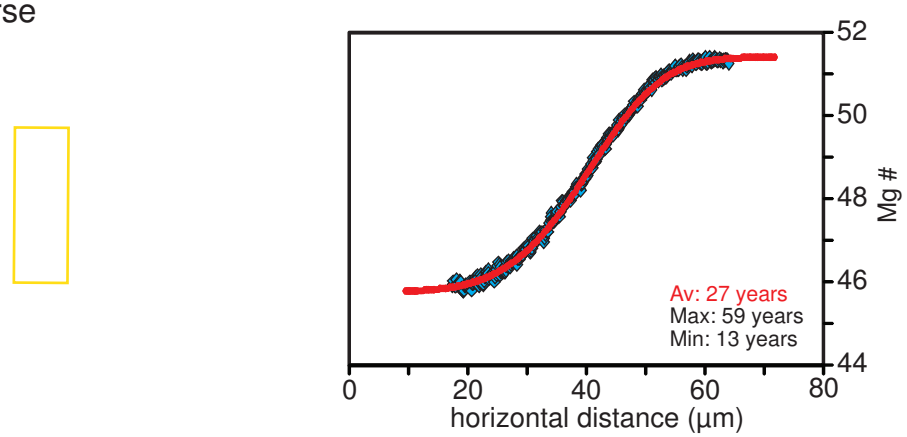

Y7_OPX12_normal

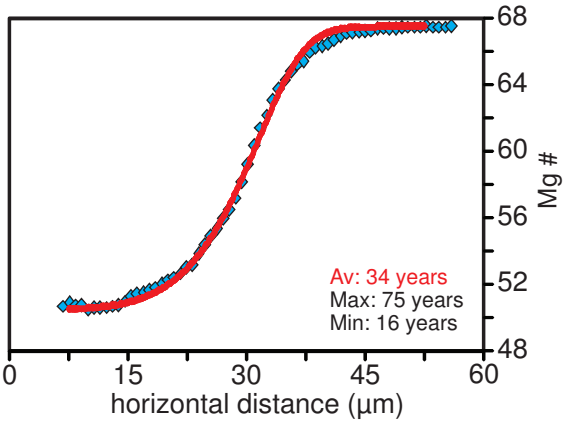

Y7_OPX11_reverse_inner

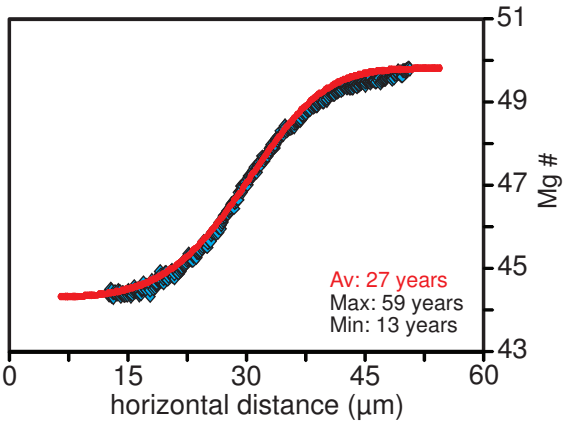

Y7_OPX11_reverse_outer

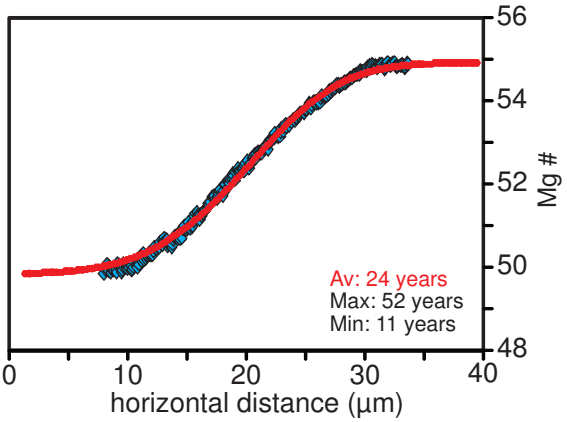

Fig. DR13. *Caption over page*

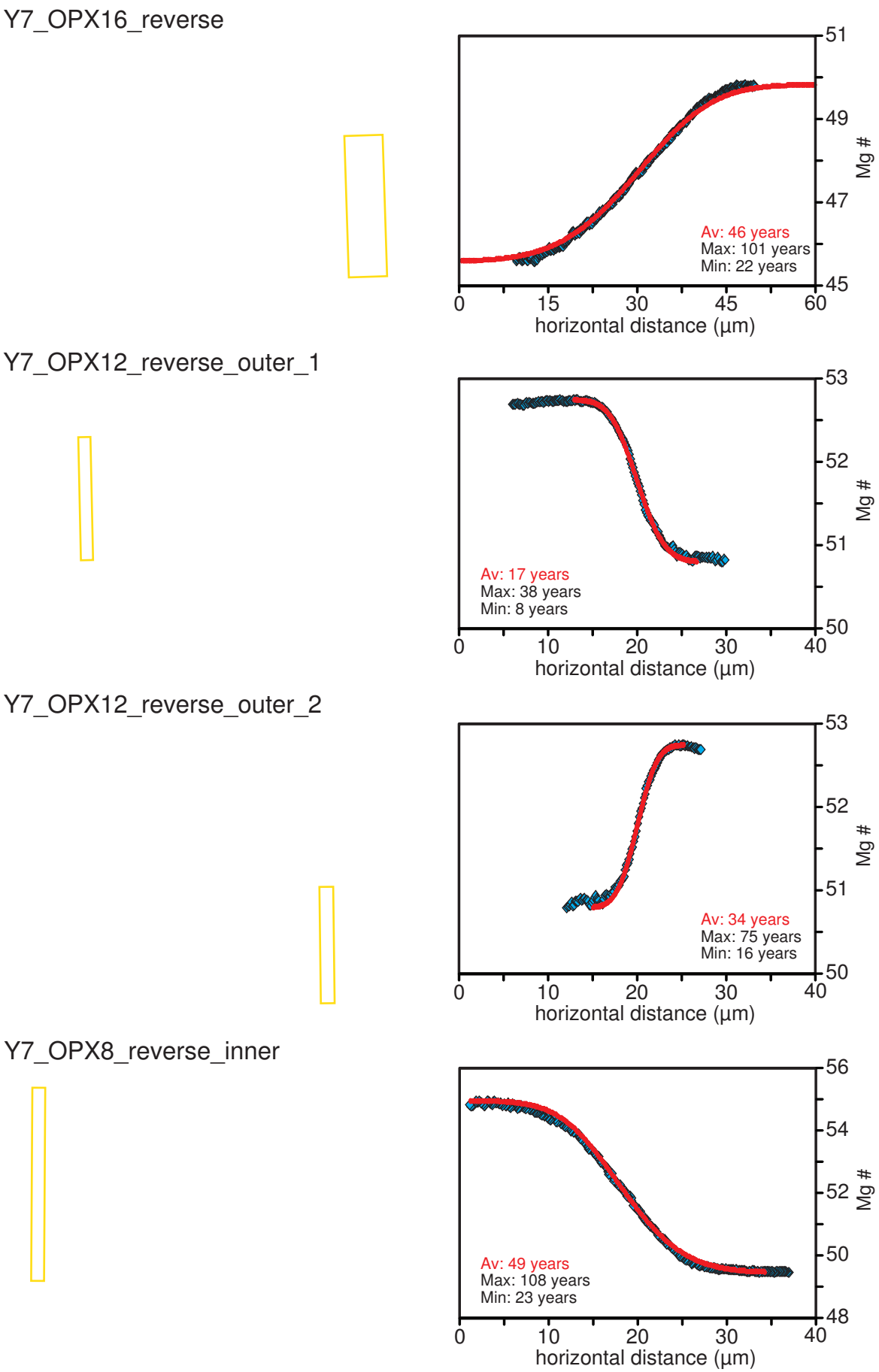

Fig. DR13. *Caption over page*

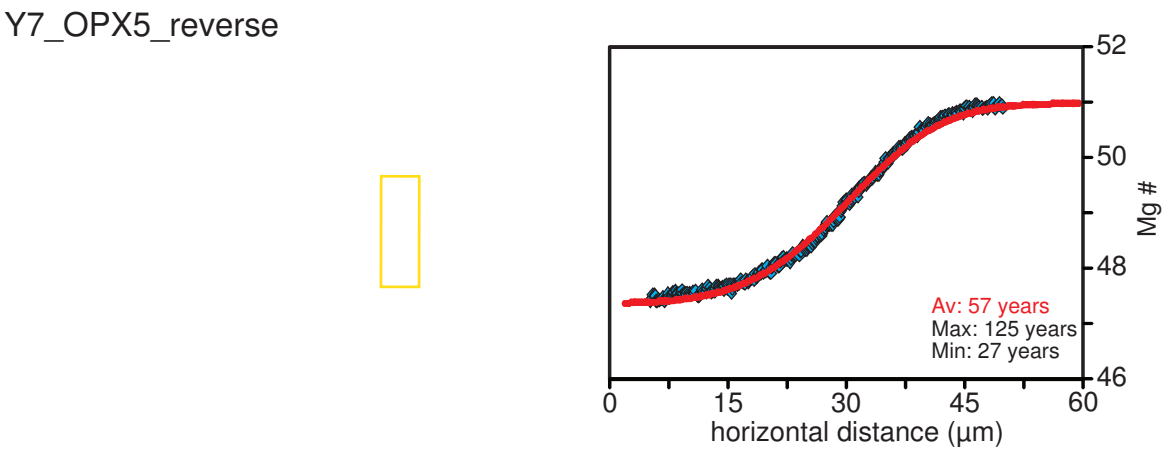

Fig. DR13. BSE images (left) and corresponding Fe-Mg diffusion models (right) of zoned orthopyroxene from Unit Y7. Average (Av) diffusion model timescales given for parameter estimates of 860 °C, 1.5 MPa and log fO_2 of 0.2 ΔNNO from Barker et al. (2015). Maximum (Max) and minimum (Min) timescales use uncertainties ±30 ºC or ± 0.3 log units Δ NNO. Other details as in Fig. DR10.

Z_OPX3_reverse_outer

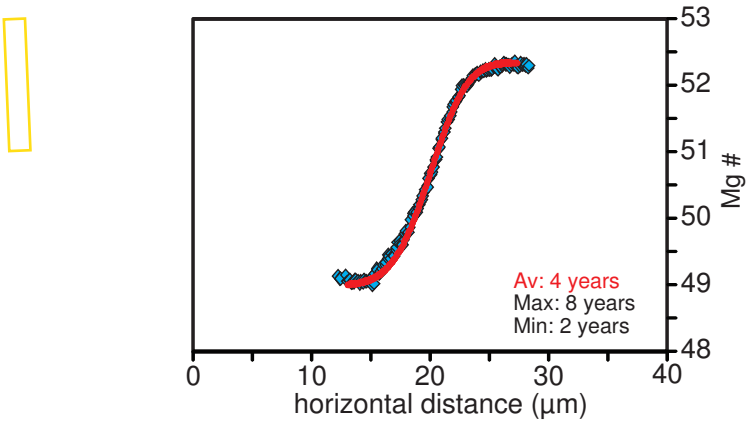

Z_OPX13_normal_outer

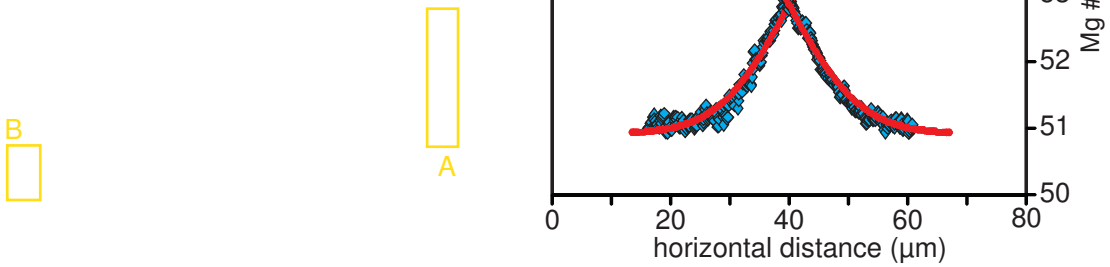

Z_OPX14_reverse

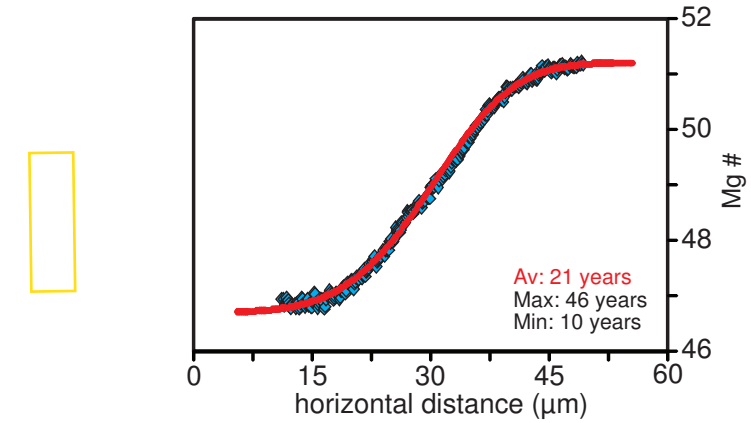

Z_OPX15_reverse

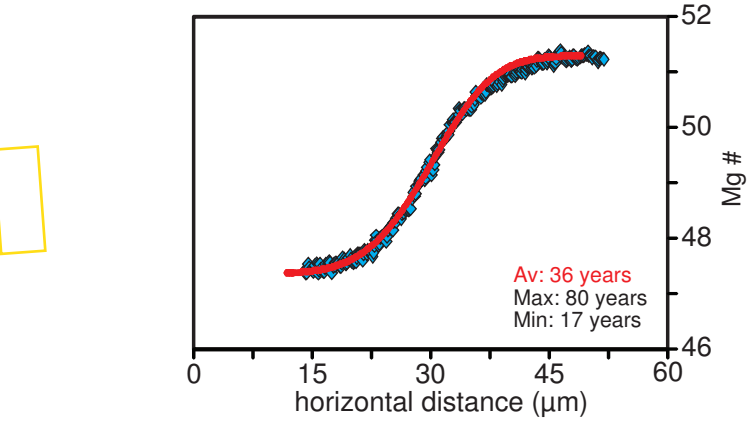

Fig. DR14. *Caption over page*

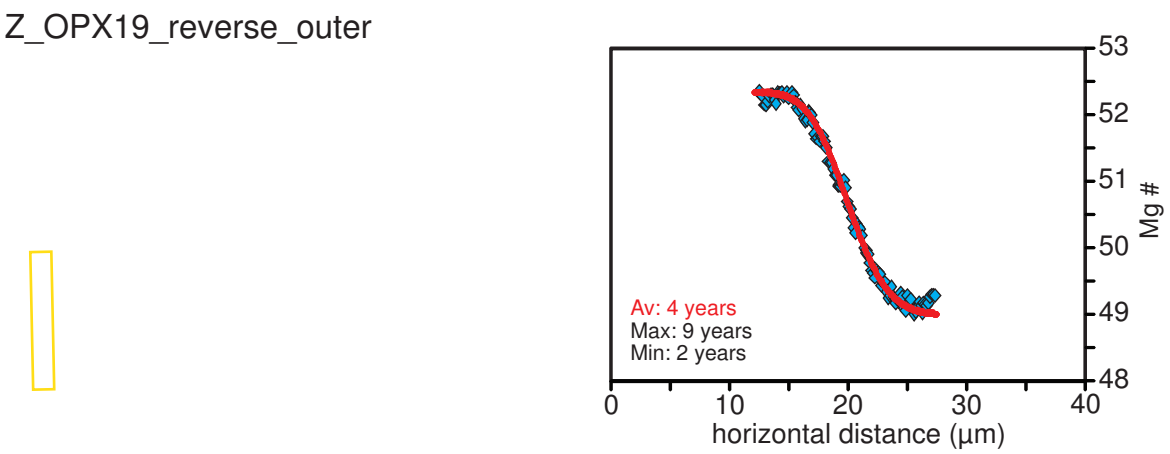

Fig. DR14. BSE images (left) and corresponding Fe-Mg diffusion models (right) of zoned orthopyroxene from eruption Z. Average (Av) diffusion model timescales given for parameter estimates of 860 °C, 1.5 MPa and log fO_2 of 0.0 ΔNNO from Barker et al. (2015). Maximum (Max) and minimum (Min) timescales use uncertainties ±30 ºC or ± 0.3 log units Δ NNO. Other details as in Fig. DR10.

REFERENCES CITED IN SUPPLEMENTARY MATERIAL

Allan, A.S.R., Morgan, D.J., Wilson, C.J.N., and Millet, M-A., 2013, From mush to eruption in centuries: assembly of the super-sized Oruanui magma body: Contributions to Mineralogy and Petrology, v. 166, p. 143-164, doi:10.1007/s00410-013-0869-2.

Barker, S.J., Wilson, C.J.N., Allan, A.S.R., and Schipper, C.I., 2015, Fine-scale temporal recovery, reconstruction and evolution of a post-supereruption magmatic system: Contributions to Mineralogy and Petrology, v. 170, article 5, doi:10.1007/s00410-015-1155-2.

Chamberlain, K.J., Morgan, D.J. and Wilson, C.J.N., 2014, Timescales of mixing and mobilisation in the Bishop Tuff magma body: perspectives from diffusion chronometry: Contributions to Mineralogy and Petrology v. 168, article 1034, doi:10.1007/s00410-014-1034-2.

Cooper, G.F., 2014, The dynamics of large-scale silicic magmatic systems: case studies from Mangakino volcanic centre, Taupo Volcanic Zone, New Zealand. PhD thesis, Victoria University of Wellington, Wellington, New Zealand.

Costa, F., and Dungan, M., 2005. Short time scales of magmatic assimilation from diffusion modeling of multiple elements in olivine: Geology, v. 33, p. 837-840, doi:10.1130/G21675.1.

Costa, F., Chakraborty, S., and Dohmen, R., 2003. Diffusion coupling between trace and major elements and a model for calculation of magma residence times using plagioclase: Geochimica et Cosmochimica Acta, v. 67, p. 2189-2200, doi:10.1016/S0016-7037(02)01345-5.

Ganguly, J., and Tazzoli, V., 1994, Fe^{2+}-Mg interdiffusion in orthopyroxene: Retrieval from the data on intracrystalline exchange reaction: American Mineralogist, v. 79, p. 930-937.

Ghiorso, M.S. and Evans, B.W., 2008, Thermodynamics of rhombohedral oxide solid solutions and a revision of the Fe-Ti two-oxide geothermometer and oxygen barometer: American Journal of Science, v. 308, p. 957-1039, doi:10.2475/09.2008.01

Giordano, D., Russell, J.K., and Dingwell, D.B., 2008, Viscocity of magmatic liquids: A model: Earth and Planetary Science Letters, v. 271, p. 123-134. doi:10.1016/j.epsl.2008.03.038.

Hogg, A.G., Lowe, D.J., Palmer, J., Boswijk, G., and Ramsey, C.B., 2011, Revised calendar date for the Taupo eruption derived by ^{14}C wiggle-matching using a New Zealand kauri ^{14}C calibration data set: Holocene, v. 22, p. 439-449, doi:10.1177/0959683611425551.

Martin, V.M., Morgan, D.J., Jerram, D.A., Caddick, M.J., Prior, D.J., and Davidson, J.P., 2008, Bang! Month-scale eruption triggering at Santorini Volcano: Science, v. 321, p. 1178, doi:10.1126/science.1159584.

Morgan, D.J., Blake, S., Rogers, N.W.B., DeVivo, B., Rolandi, G., Macdonald, R., and Hawkesworth, C.J., 2004, Time scales of crystal residence and magma chamber volume from modelling of

diffusion profiles in phenocrysts: Vesuvius 1944: Earth and Planetary Science Letters, v. 222, p. 933-946, doi:10.1016/j.epsl.2004.03.030.

Morgan, D.J., Rogers, N.W., Blake, S., De Vivo, B., Rolandi, G. and Davidson, J.P., 2006, Magma recharge at Vesuvius in the century prior to AD79: Geology, v. 34, p. 845-848, doi:10.1130/G22604.1.

Putirka, K., 2008, Thermometers and barometers for volcanic systems: Reviews in Mineralogy and Geochemistry, v. 69, p. 61–111. doi:10.2138/rmg.2008.69.3.

Sauerzapf, U., Lattard, D., Burchard, M. and Engelman, R., 2008, The titanomagnetite-ilmenite equilibrium: new experimental data and thermo-oxybarometric application to the crystallization of basic to intermediate rocks: Journal of Petrology, v. 49, p. 1161-1185, doi:10.1093/petrology/egn021.

Saunders, K., Blundy, J., Dohmen, R., and Cashman, K., 2012, Linking petrology and seismology at an active volcano: Science, v. 336, p. 1023-1027, doi:10.1126/science.1220066

Wark, D.A., Hildreth, W., Spear, F.S., Cherniak, D.J., and Watson, E.B., 2007, Pre-eruption recharge of the Bishop magma system: Geology, v. 35, p. 235-238, doi:10.1130/G23316A.1.

Wilson, C.J.N., 1993, Stratigraphy, chronology, styles and dynamics of late Quaternary eruptions from Taupo volcano, New Zealand: Philosophical Transactions of the Royal Society of London, ser. A, v. 343, p. 205-306, doi:10.1098/rsta.1993.0050.

Zellmer, G.F., Blake, S., Vance, D., Hawkesworth, C. and Turner, S., 1999, Plagioclase residence times at two island arc volcanoes (Kameni Islands, Santorini, and Soufriere, St. Vincent) determined by Sr diffusion systematics: Contributions to Mineralogy and Petrology, v. 136, p. 345-357, doi:10.1007/s004100050543.